Reaction-Path Dynamics Study of the Thermal Unimolecular Reactions in the Gas Phase: Branching and Selectivity of the Reaction Path

気相における単分子熱反応の反応経路動力学の研究: 反応経路の分岐と選択性

岡田 和正

Reaction-Path Dynamics Study of the Thermal Unimolecular Reactions in the Gas Phase: Branching and Selectivity of the Reaction Path

A Dissertation
Submitted to the Faculty of Science
in Partial Fulfillment of the Requirements
for the Degree of

Doctor of Science

at

HIROSHIMA UNIVERSITY

1996

By

Kazumasa Okada

To Mr. M. Hiraoka

Preface

This is a dissertation submitted to the Faculty of Science, Hiroshima University. The material for this dissertation is the product of the author's studies in the doctoral course, which is the continuation of his studies in the undergraduate senior and master's courses.

As mentioned at length in the text, a method of chemical activation has come to be known since 1960, and has been used extensively by Rabinovitch and co-workers. They used bimolecular reactions such as additions of atoms and radicals to olefins for preparing molecules at high levels of excitation, whereas in this laboratory chemical activation by unimolecular decompositions was found and has been studied vigorously to interpret their dynamical behaviors.

In the meantime, the electronic theory of chemical reactions has served us well for understanding the reaction mechanisms and dynamics. In 1980 Miller, Handy, and Adams derived the Hamiltonian for a reacting molecular system based on the intrinsic reaction coordinate of Fukui. This model has been applied to some reactions of small systems, and has acquired great success to interpret the experimental results regarding the product state distributions.

The main theme of this thesis is placed at the connection between the dynamical features of chemical reactions and the characteristics of the potential energy surfaces. Some reactions showing branchings of products are examined both experimentally and

theoretically by means of the above-mentioned techniques. The author believes that this is the first application to such reactions and is a highly successful attempt. It is an unexpected pleasure for him if this thesis is read and referred to by many researchers.

The author should like to take this opportunity to express his cordial gratitude to Professor K. Saito for his kind guidance, valuable suggestions, stimulating discussions, and constant encouragement. He is indebted to Professor A. Imamura for his own introduction to molecular orbital theory and to Dr. S. Yabushita for his helpful advice and discussions about computations. He also appreciates suggestive comments from Dr. K. Tabayashi, Mr. O. Takahashi, and many other members of the laboratory. The numerical calculations were carried out at the Information Processing Center of Hiroshima University and the Computer Center of the Institute for Molecular Science (IMS). The author thanks the Centers for allocating CPU time. Last, but foremost, he wishes to express his appreciation to his parents for their every support as well as their unfailing love and affection.

This manuscript was typeset with the LaTeX version 2.09 document preparation system.

Contents

Reaction-Path Dynamics Study of the Thermal Unimolecular Reactions in the Gas Phase: Branching and Selectivity of the Reaction Path

Kazumasa Okada

Chapter 1

Prolegomena

It is one of the most important subjects in chemistry to understand chemical reactions as systematically as possible. One way to approach this is chemical kinetics or reaction dynamics. Chemical change is analyzed rigorously to find a law that regulates chemical reactions. It is principally possible to discuss a chemical reaction, however complicated, by resolving into the composite elementary processes. Much effort has been devoted to devise a new technique with which reaction process is studied microscopically. Different experimental approaches have been developed to study elementary reactions. In recent years more interest has been directed toward understanding the mechanisms and rates of intramolecular vibrational energy redistribution (IVR) [1–3]. This interest has intensified with the introduction and application of lasers. The advent of molecular beams and pulsed laser techniques has produced a new branch of chemistry, i.e., "state-to-state" chemistry.

Accumulation of experimental results by such reaction studies stimulates the electronic theory for chemical reactions, and rapid progress has been made in this field. The advancement of computer technology, coupled with the development of molecular orbital theory itself, has greatly improved the accuracy and reliability of electronic structure the-

ory, which, in turn, has motivated new experimental works. Ab initio molecular orbital computations constitute the integral part of the current theoretical studies for chemical reactions.

We have paid our attention to several gas-phase thermal unimolecular decompositions of relatively large molecules. The objective is to explore the consecutive reaction of an intermediary formed fragment rather than to determine the decomposition route and rate of a parent reagent. Of particular interest is mode-selective control of the reaction pathway by selective excitation employing a method of chemical activation. To this end, it is quite necessary to get information from the theoretical side. Therefore, we have performed theoretical calculations as well as shock tube experiments.

The organization of the present dissertation is as follows. In Chapters 2 and 3, we will explain the experimental and the theoretical approaches employed in this study. In Chapter 2, a technique of chemical activation and the concrete results of works done so far in our laboratory will be introduced to emphasize that this technique is very useful for us to investigate the dynamical features of chemical reactions. A theoretical approach that offers an interpretation of dynamics by analyzing the topography of the potential energy surface will be given in Chapter 3. Chapters 4 through 6 describe the results and discussion for the individual reaction system pursued in the present study. Finally, general conclusion and future prospects will be presented in Chapter 7.

Chapter 2

Experimental Approach

2.1 Method of Chemical Activation

It is well established that most experimental rate data are adequately described by statistical theory of reaction: RRKM theory is one of such theories. On the other hand, it is clear that non-statistical behavior can occur in many systems, even though it is not manifested in most experiments. When excitation energy is placed in a particular mode, it flows out along the specific pathways. If a non-statistical distribution of energy persists for times comparable or long relative to that required for reaction, mode selectivity in the reaction can result. Methods such as chemical activation, hot-atom reactions, photoactivation, and molecular beams can produce non-statistical distributions of energy in energized species, and they often provide direct tests of the hypothesis of energy randomization in statistical theory [4–7].

Chemical activation is a technique with which energized species is prepared by a chemical reaction [2, 4, 5]. It was proposed by Butler and Kistiakowsky [8] and by Rabinovitch and co-workers [9] in 1960. It is a useful technique because it provides vibrationally

excited species having high energies within a relatively narrow, well-defined region of energy, and yields information on threshold energies, thermochemical data, energy transfer data [6], and energy partitioning [10]. Energized species have been obtained by various reactions and, in particular, the addition of CH_2 to olefins has been used to produce molecules with high energy (40–100 kcal/mol) [11–13]. By using different association or addition reactions, the same complex can be produced in different states of vibrational excitation at a particular temperature.

If more than one reaction channel is available for reaction, the large excess energy in chemical activation makes processes observable which in conventional thermal studies would not be detected, because of their high activation energies. To take an example from recent studies, Arbilla et al. [14] reported the chemical activation study of 1-methyl-2,2,3,3-tetrafluorocyclopropane. Isomerization occurs in competition with decomposition, only the latter being observed in the conventional thermal study.

Chemical activation is potentially a site-selective technique, as elegantly demonstrated by Rabinovitch and co-workers [15–19]. For example, addition of CD_2 to hexafluorovinylcyclopropane (1) produces hexafluorobicyclopropyl (2), in which the newly formed ring is labeled with deuterium [15]:

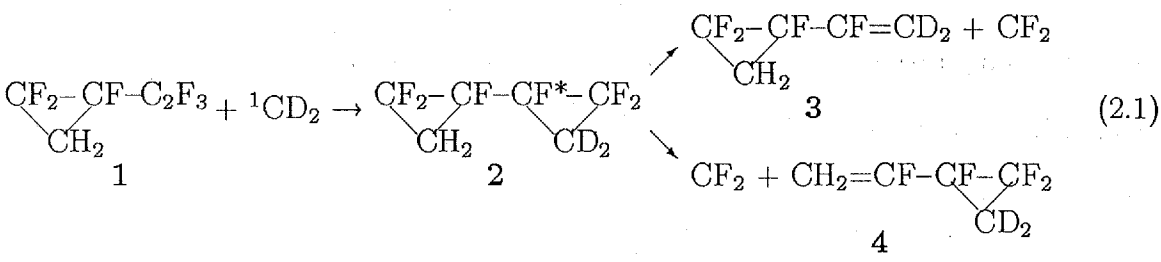

1 2 3 4 (2.1)

They found that increasing pressure, which means a decrease in time available for 2 to react, causes the ratio [3]/[4] to increase, showing that the newly formed ring (*hot* ring) opens preferentially. The result was confirmed by reversing the isotopic labeling.

2.2 Chemical Activation Studies in Our Laboratory

As mentioned in the previous section, chemical activation has been a powerful technique in studying unimolecular reactions and intramolecular energy-transfer processes. In contrast to the conventional bimolecular reactions, from past studies in our laboratory thermal unimolecular decompositions of relatively large molecules were found to produce activated species with specific energy disposal. The fragment molecules produced by such reactions show peculiar selectivity for the consecutive reaction paths and/or have different rate constants, compared to the reactions starting with the stable fragment molecules as reactants.

Previously, the thermal decomposition of carboxylic esters were investigated in our laboratory using a shock tube. It is well known that the unimolecular pyrolysis of formic acid occurs through two competing channels; decarboxylation leading to carbon dioxide and molecular hydrogen (2.2a), and dehydration leading to water and carbon monoxide (2.2b):

$$HCOOH \rightarrow CO_2 + H_2 \,, \tag{2.2a}$$

$$\rightarrow H_2O + CO \,. \tag{2.2b}$$

The branching ratio of decarboxylation to dehydration is 0.02 at around 1500 K [20]. On the other hand, formic acid can be prepared by the pyrolysis

$$HCOOC_2H_5 \rightarrow HCOOH + C_2H_4 \tag{2.3}$$

and branching ratio for the consecutive reaction channels 2.2a and 2.2b was determined to be 0.125–0.135 under the same conditions [21]. The channel 2.2a becomes preponderant with decreasing the total pressure, although the potential barrier for channel 2.2a is higher than that of channel 2.2b. Remarkable difference between each other indicates that a

formic acid molecule produced by the pyrolysis of ethyl formate is chemically activated and has specific vibrational energy distributions which affect the consecutive reaction to a considerable extent.

Similarly, the thermal decomposition of ethyl acetate has been investigated as well [22]. Contrary to our expectations, the result was obtained opposite to that for ethyl formate. A discussion about this is left over until Chapter 7.

More recently, we conducted the thermal decomposition of acetaldoxime in the temperature range 933–1183 K [23]. Production of methyl isocyanide was observed by monitoring IR emission from its fundamental band, i.e., at 4.6 μm (NC stretching mode). Figure 2.1 shows typical IR emission–time traces. It was found that in this reaction there exists a pathway leading directly to methyl isocyanide by comparing time-dependent emission intensities of acetonitrile and methyl isocyanide, as illustrated in Figure 2.1.

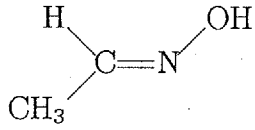

$$\rightarrow \mathrm{CH_3CN/CH_3NC + H_2O} \tag{2.4}$$

Production of methyl isocyanide can be detected at much higher temperatures for the thermal isomerization of acetonitrile [24]. It is therefore inferred that an acetaldoxime molecule undergoing decomposition has a special structure and energy partitioning leading preferentially to methyl isocyanide.

The outcome of these findings means that a technique using a shock tube is highly useful for us to study reactions which have dynamically interesting features. We will consider some reaction systems in which nitriles are produced by the thermal decompositions as candidates, and will discuss each system in Chapters 4 through 6.

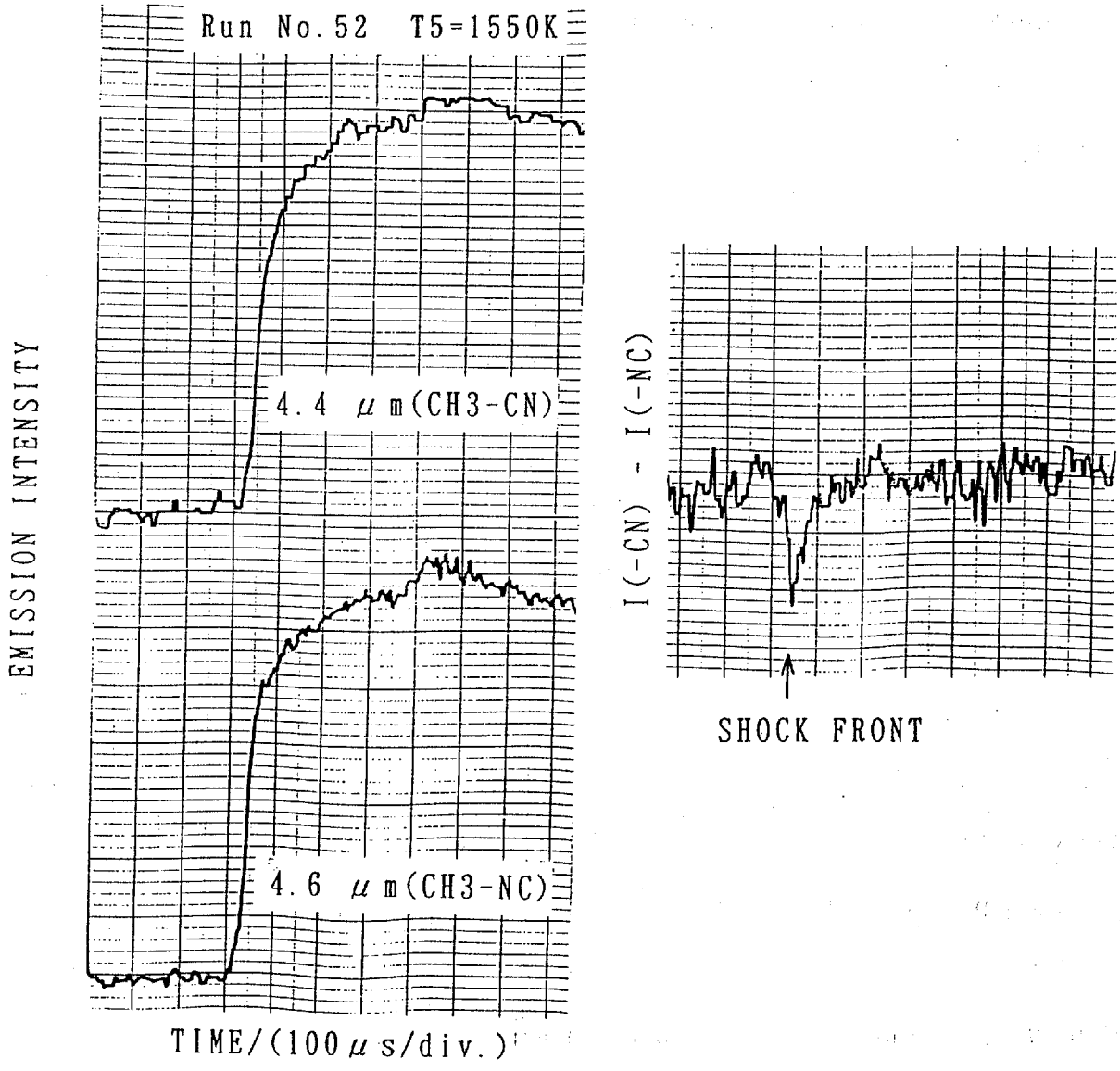

Figure 2.1: Typical IR emission traces. Right profile shows the difference of emission intensities.

Chapter 3

Theoretical Methodology

3.1 Reaction Paths

Understanding of a chemical reaction at a microscopic level requires, in addition to knowledge about reactant(s), products, and transition states, detailed information on the reaction processes, i.e., the reaction path connecting the stationary points on the potential energy surface. A convenient definition of the reaction path for a polyatomic reaction is to start at the saddle point and follow the steepest descent path in mass-weighted coordinates, forward to products and backward to reactant(s): the intrinsic reaction coordinate (IRC) path was suggested and has been popularized by Fukui [25,26].

The IRC is defined by the solution of Newton's equations of motion, under the constraint that the velocity at any point along the path is zero. An equivalent view of this path is as a steepest descent path in mass-weighted coordinates, with the initial descent direction being taken to be the transition vector:

$$\frac{d\boldsymbol{x}(s)}{ds} = -\frac{\boldsymbol{g}}{g} \tag{3.1}$$

where g is the energy gradient and s is the distance along the path. Because of zero kinetic

energy throughout the trajectory the IRC does not correspond to any real trajectory but probes an important swath of the potential energy surface. The description of chemical reactions in terms of the IRC has been extensively investigated by Fukui and collaborators [27,28]. To date, various methods for computing reaction paths have been proposed [29–35] (see also Ref. 36).

While valuable insights into the reaction mechanisms can be gained by determining the changes in the molecular structure along the reaction path, a detailed understanding of the dynamics of chemical reactions requires additional information on the molecular potentials.

3.2 Reaction-Path Hamiltonian

The study of some aspects of reaction dynamics using ab initio potential energy surfaces has been considerably advanced by the introduction of reaction-path Hamiltonian based methods. The physical model has been introduced by Hofacker [37] and by Marcus [38] for A + BC → AB + C reactions and developed by Miller, Handy, and Adams for general nonlinear polyatomics [39]. The coordinates of the reaction-path Hamiltonian model are the reaction coordinate and the normal-mode coordinates for vibrations transverse to the IRC. One of the important practical aspects of this model is that all of the frequencies necessary to define it are obtainable from a relatively modest number of computational calculations. The growing number of dynamical studies of polyatomic systems based on the reaction-path Hamiltonian have been made [40–43], and have been reviewed by Miller [44] and by Truhlar and co-workers [45–47].

Of the $3N$ nuclear degrees of freedom, six correspond to the overall external motion (translation and rotation) of the whole system, and one to the motion along the IRC.

The remaining $3N-7$ transverse modes should be orthogonal to the external modes and to the IRC motion. If we perform a local normal-mode analysis pointwise along the IRC by first calculating the matrix of the second derivatives in mass-weighted Cartesian coordinates, eliminating the coupling between transverse and external modes by applying an appropriate projection procedure [39], and diagonalizing the resulting modified force constant matrix, we obtain the $3N-7$ transverse vibrational harmonic frequencies $\omega_k(s)$ and the corresponding eigenvectors $\boldsymbol{L}_k(s)$ as functions of the reaction coordinate s.

If s and p_s are the reaction coordinate (the mass-weighted distance along the IRC) and its conjugate momentum, and (Q_k, P_k), $k = 2, ..., F$ are the normal mode coordinates and momenta for vibrations orthogonal to the IRC ($F = 3N-6$ is the number of degrees of freedom in the N-atom system), then the classical reaction-path Hamiltonian for total angular momentum $J = 0$ in the vicinity of the IRC is given by

$$H(s, p_s, \{Q_k, P_k\}; k = 2, \ldots, F) = \sum_{k=2}^{F} \left[\frac{1}{2}P_k^2 + \frac{1}{2}\omega_k(s)^2 Q_k^2\right] + V_0(s) + \frac{1}{2}\frac{\left[p_s - \sum_{k,k'=2}^{F} Q_k P_{k'} B_{k,k'}(s)\right]^2}{\left[1 + \sum_{k=2}^{F} Q_k B_{k,1}(s)\right]^2} \tag{3.2}$$

$V_0(s)$ is the potential energy along the IRC, and $\{\omega_k(s)\}$ are the local transverse vibrational frequencies as a function of the reaction coordinate. $\{B_{k,k'}(s)\}$ are the coupling elements between one vibrational mode and other, and between each vibrational mode and reaction coordinate (labeled as mode $k = 1$). The last term is the kinetic energy for motion along the reaction coordinate plus coupling between the various transverse modes. These coupling elements are given explicitly by

$$B_{k,k'}(s) = \frac{\partial \boldsymbol{L}_k(s)}{\partial s} \cdot \boldsymbol{L}_{k'}(s) \tag{3.3}$$

where $\boldsymbol{L}_k(s)$ is again the eigenvector of the projected force constant matrix for mode k.

$L_1(s)$ is the normalized gradient vector which is the direction along the reaction coordinate. The coupling elements $B_{k,1}(s)$, $k = 2, ..., F$, are a measure of how the curvature of the IRC couples to the transverse mode k, and the total curvature of the IRC is related to these elements by

$$\kappa(s) = \left(\sum_{k=2}^{F} B_{k,1}(s)^2 \right)^{1/2} \tag{3.4}$$

The internal centrifugal force caused by the curvature $\kappa(s)$ pushes the real trajectory away from the IRC and gives rise to excitations in the motion of the Q_k's. Mixing of different vibrational modes, and therefore energy transfer between the reaction coordinate and other modes, takes place in the region where $\kappa(s)$ is large. The elements $B_{k,k'}(s)$, are Coriolis-like couplings related to how much modes k and k' spiral about the reaction path as s varies.

3.3 Computational Details

In a series of studies herein, ab initio molecular orbital (MO) calculations were implemented using the GAUSSIAN 86 [48], GAUSSIAN 88 [49], GAUSSIAN 90 [50], and GAUSSIAN 92 [51] program packages. We used 3-21G basis set, except in Chapter 6 where two types of basis sets, labeled 3-21G and 6-31G** were employed. The equilibrium and transition-state geometries were fully optimized at the Hartree–Fock level using the energy gradient technique. Harmonic vibrational frequencies at the stationary points were evaluated using analytical second derivatives in order to estimate zero-point vibrational energies and to characterize the stationary points.

In an attempt to obtain an insight into the dynamical features of the reaction, we then constructed the IRC at the HF/3-21G level with a step-size of 0.10 $\sqrt{\text{amu}}$ bohr. Along this IRC, the reaction coordinate s is defined as the signed distance from the saddle

point, with $s < 0$ referring to the reactant side. The vibrational frequency analyses along the IRC were carried out to obtain the coupling elements and the curvature of the IRC. At each non-stationary point along the IRC, the local vibrational frequencies $\omega_k(s)$ transverse to the IRC and the corresponding eigenvectors $\boldsymbol{L}_k(s)$ can be obtained by diagonalizing the projected force constant matrix, after projecting out the motion along the IRC as well as overall translations and rotations. This was made by applying the method of Miller et al. (generalized normal-mode analysis) [39]. The coupling elements involve the first derivatives of the eigenvectors with respect to the reaction coordinate s. They are calculated by the numerical finite difference method:

$$\frac{\partial \boldsymbol{L}_k(s)}{\partial s} = \lim_{\delta s \to 0} \frac{\boldsymbol{L}_k(s+\delta s) - \boldsymbol{L}_k(s)}{\delta s}, \tag{3.5}$$

In practice, in Eq. (3.5) the increment δs is taken along the energy gradient direction $\boldsymbol{g}(s)$ as ± 0.0001. If the IRC motion is labeled by $k = 1$, the total curvature of the IRC $\kappa(s)$ is the norm of the vector composed of the coupling elements $B_{k,1}$ (Eq. 3.4).

While a rationale for the qualitative features of reaction dynamics is provided by an analysis of the coupling terms, the actual influence of the terms on the reaction should be confirmed by trajectory calculations. For the trajectory calculations, the conventional method is to calculate the reaction probability etc. statistically from the trajectories in which various initial conditions are determined by Boltzmann distribution at a given temperature [52]. Here, we instead carried out in order to verify how a particular geometry and a specific vibrational mode of the molecule during the course of the reaction are related to the reaction path. The calculation of the classical trajectory was done as follows. First we calculate the potential energy and gradient at the initial point. This determines forces on the constituent atoms at this point. The integration is carried out over the small time interval, and the final point of this trajectory becomes the initial point for the local

trajectory in the next iteration. The potential and kinetic energies and gradient are calculated at this new coordinate, and then a new local trajectory is calculated. This sequence is repeated until the trajectory is completed. The algorithm utilized is the same as the DRC subroutine [53] incorporated within the MOPAC program package [54].

Chapter 4

Thermal Unimolecular Decomposition of Acetaldoxime

4.1 Introduction

In this chapter, we examine the dynamical behavior of the unimolecular decomposition process of acetaldoxime, of which experimental result is summarized in Section 2.2, by means of ab initio MO calculations. We will study according to the method described in Chapter 3, and consider the bifurcation point toward thermochemically less stable methyl isocyanide on the potential energy surface for this reaction system.

The energy transfers in the chemical reaction are analyzed with respect to nuclear motion along the IRC and vibrational motions transverse to the IRC. Such treatments have first been exploited to the product energy partitioning in the unimolecular elimination reactions [55].

4.2 Results and Discussion

4.2.1 IRC analysis

Figure 4.1 shows the full-optimized geometry of the transition state and the displacement vectors along the reaction coordinate. Geometrical changes along the IRC are shown in Figure 4.2. Since the IRC is a static reaction path as the trajectory of the zero kinetic energy starting from the transition state, it leads to the thermochemically favorable products, acetonitrile and water.

The variation of the frequencies along the IRC is plotted in Figure 4.3. The step size of calculation was $\Delta s = 0.10\ \sqrt{\text{amu}}$ bohr. The numbering of the vibrational modes follows the convention at the transition state. On connecting these points, we adopted the following criteria of crossing or noncrossing: two points which are similar in the displacement vectors are connected, and the discontinuous change should not occur in the vibrational modes. Therefore, our treatment corresponds to the one based on the "diabatic" or "nonadiabatic" representation of vibrational modes [56]. The vibrational frequency for the C–N stretching (mode 7) increases in the product indicating the formation of a C–N triple bond, and that for H_2O symmetric stretching (mode 6) changes substantially due to the formation of a new O–H bond.

The nonadiabatic couplings of vibrational modes due to the curvature of the IRC are represented by the coupling elements $B_{k,1}(s)$, which cause the energy transfer from the curving of the IRC to the particular normal modes. Figure 4.4 displays some typical coupling elements that change appreciably and curvature κ as a function of the reaction coordinate. It is seen that κ has a maximum around $s = 0.40\ \sqrt{\text{amu}}$ bohr, where the Q_6 and Q_{16} modes couple strongly to the IRC. The most active energy transfer between the IRC and these modes should take place in this region. Figure 4.5 shows these modes at

$s = 0.40$. The rise in $B_{6,1}$ is caused by the motion of the hydrogen atom associated with the formation of water. It is noted that Q_{16} is associated with a CCN bending mode. Therefore, it could be considered that a large amount of energy supply into this specific mode would make some of the trajectories to bifurcate the IRC to follow the course of the CH_3NC production.

To confirm this behavior, classical trajectory calculations are performed as described in the next section.

4.2.2 Reduction of the system and classical trajectories

In order to study the dynamics of the considered reaction system, a number of trajectories should be propagated for a range of initial kinetic energies. In the interest of computational time, here the trajectory calculations were carried out for the simplest formaldoxime reaction system. The same procedure as described in the previous section was also done for this system. The transition-state geometry was taken from the previous ab initio calculations [57]. The variation of vibrational frequencies along the IRC is shown in Figure 4.6. Figure 4.7 gives the curvature of the IRC and some of the coupling elements. Comparing these two figures with those for acetaldoxime (Figures 4.3 and 4.4), we think that the substitution of a hydrogen atom for the methyl group makes no change in the characteristic features of the reaction.

In the formaldoxime system, the strong coupled modes are modes 4 and 7. The former is concerned mainly with the vibration of the H_2O fragment. Mode 7, on the other hand, concerns HCN bending motion as in the case of mode 16 in the acetaldoxime system. Trajectories were initiated at $s = 0.40$ with an initial internal velocity vector in the direction of mode 7. The rearrangement process of the HNC fragment was traced during the course of the decomposition of the parent molecule. The initial geometry

and the components of mode 7 are given in Table 4.1 and Figure 4.8. The trajectory led to the rearrangement to hydrogen isocyanide when an initial kinetic energy of more than 100 kcal/mol was given to mode 7. Figure 4.9 illustrates the geometrical changes of the decomposing molecule with time. The actual thermal system includes kinetic energy along the reaction coordinate, and under the present initial conditions a large amount of energy was flowed into the strongly coupled reaction coordinate mode. Thus the value of 100 kcal/mol is considered to be the upper limit for the present calculation. Figure 4.10 indicates the potential energy change as a function of time from the start point of $s = 0.40$. On the other hand, there was no rearrangement when the other modes were given the same kinetic energy. In this case, the destiny of the excess kinetic energy is the consumption as the other vibrational excitation and the translational energy of the two fragments. For mode 5, for example, the geometrical changes are given by Figure 4.11, energy being consumed mainly by the C–N stretching and slightly by the relative translations. More sophisticated calculations employing better basis sets may lead to lower kinetic energy requirements for the bifurcation to occur. At the present stage, we confirmed at least that some of the trajectories proceed to the isocyanide, the thermochemically less stable product.

4.3 Summary

The dynamic decomposition process of acetaldoxime is successfully simulated by the combined approach of the IRC and classical trajectory calculations. The IRC calculation indicates that curvature of the reaction path is considerable in the vicinity of $s = 0.40\sqrt{\text{amu}}$ bohr, and in particular that this curvature strongly couples the reaction coordinate to the CCN bending mode. Classical trajectory calculations initiating

at this point with an excess kinetic energy on the HCN bending mode confirm that the decomposition leads to the arrangement of the isocyanide in the case of the formaldoxime system.

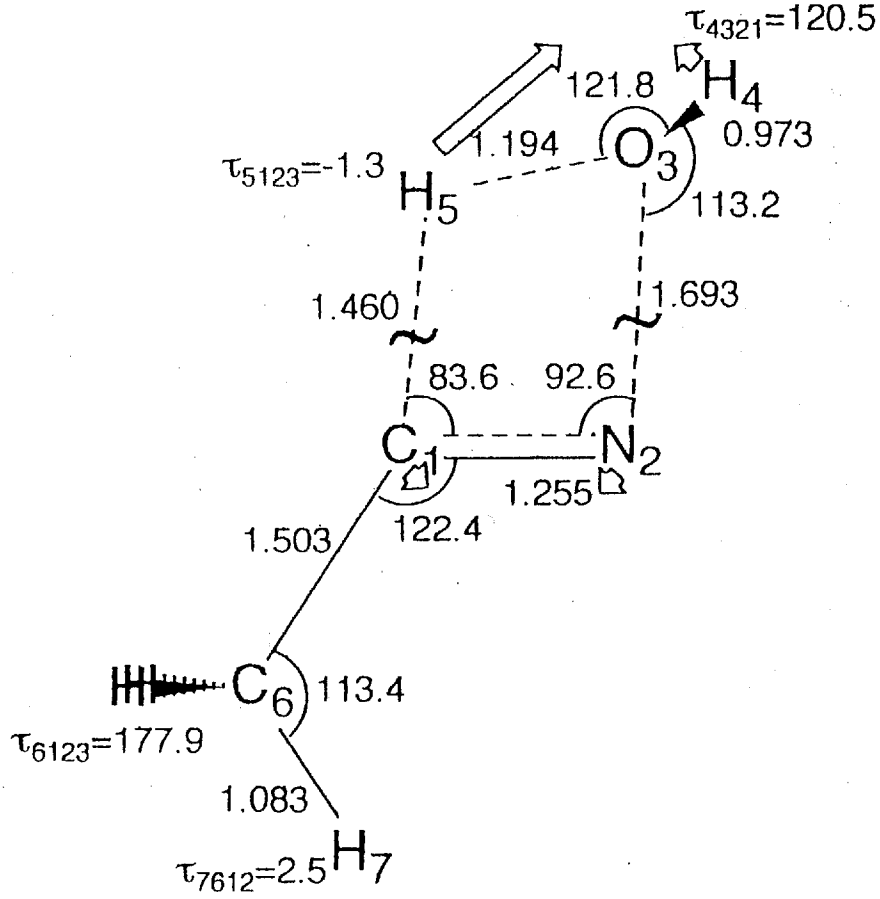

Figure 4.1: HF/3-21G optimized geometry of the transition state for the decomposition of acetaldoxime. Bond distances are in angstroms and angles are in degrees. The arrows are displacement vectors of the normal mode along the reaction coordinate ($1978i$ cm^{-1}).

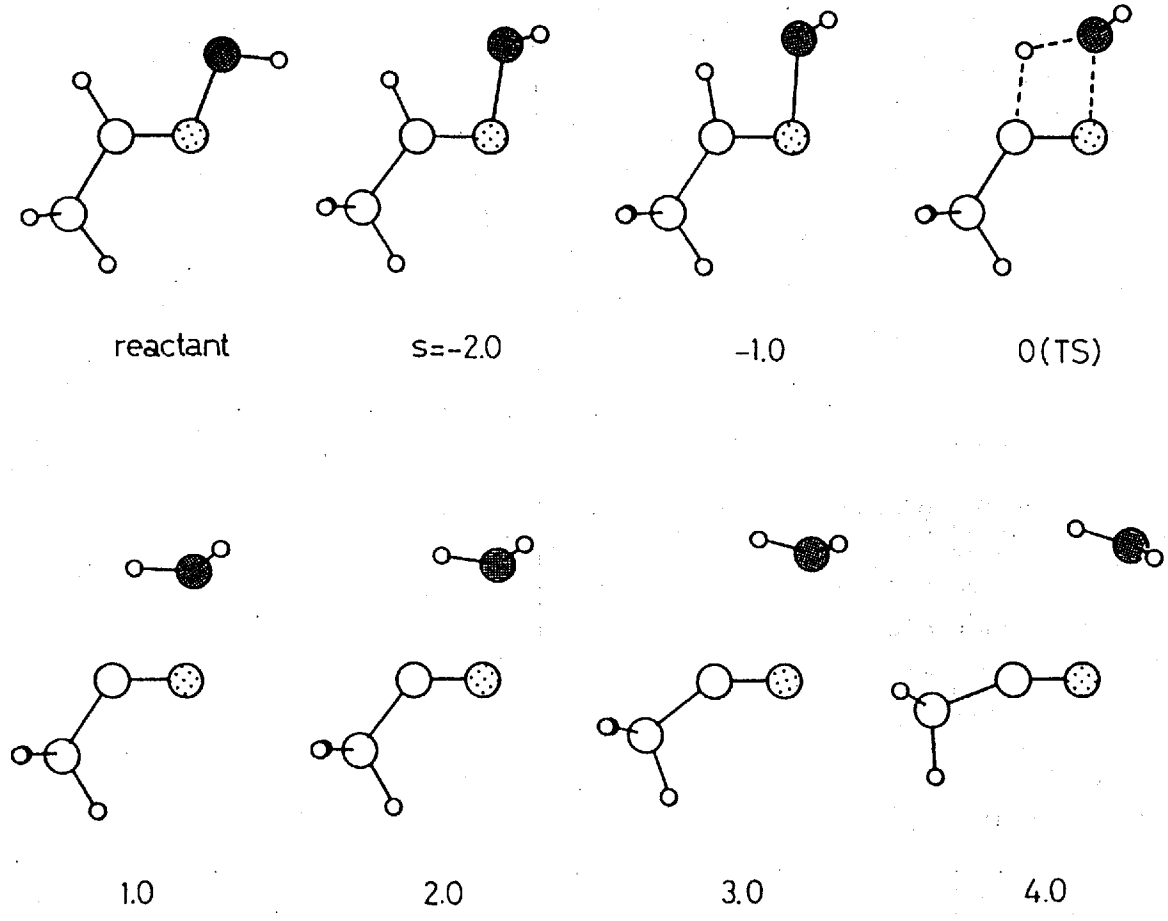

Figure 4.2: Geometrical changes along the IRC for the decomposition of acetaldoxime. Indicated values represent the reaction coordinate.

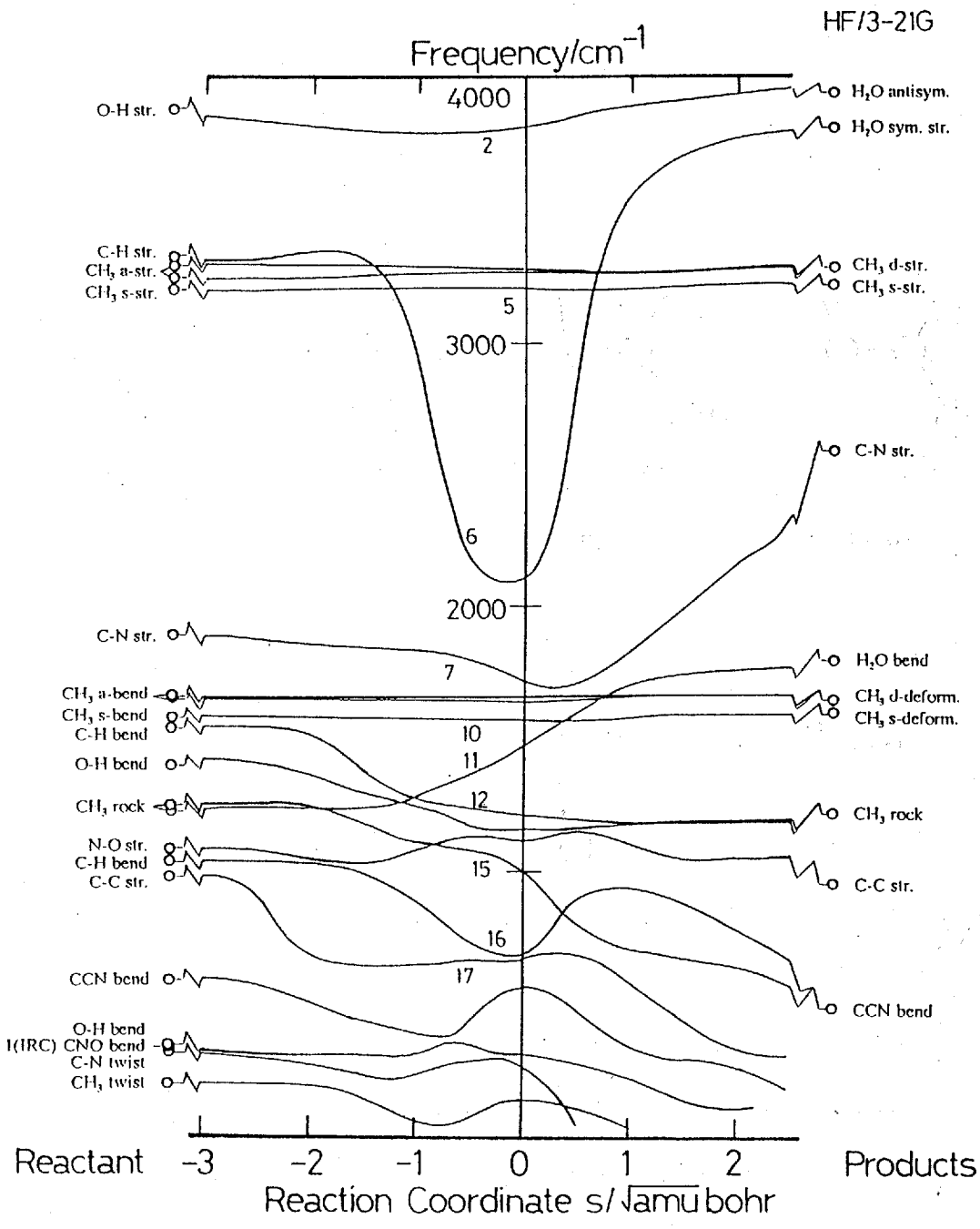

Figure 4.3: Variation of the projected frequencies along the IRC for the decomposition of acetaldoxime. The modes are labeled as appropriate for the transition state.

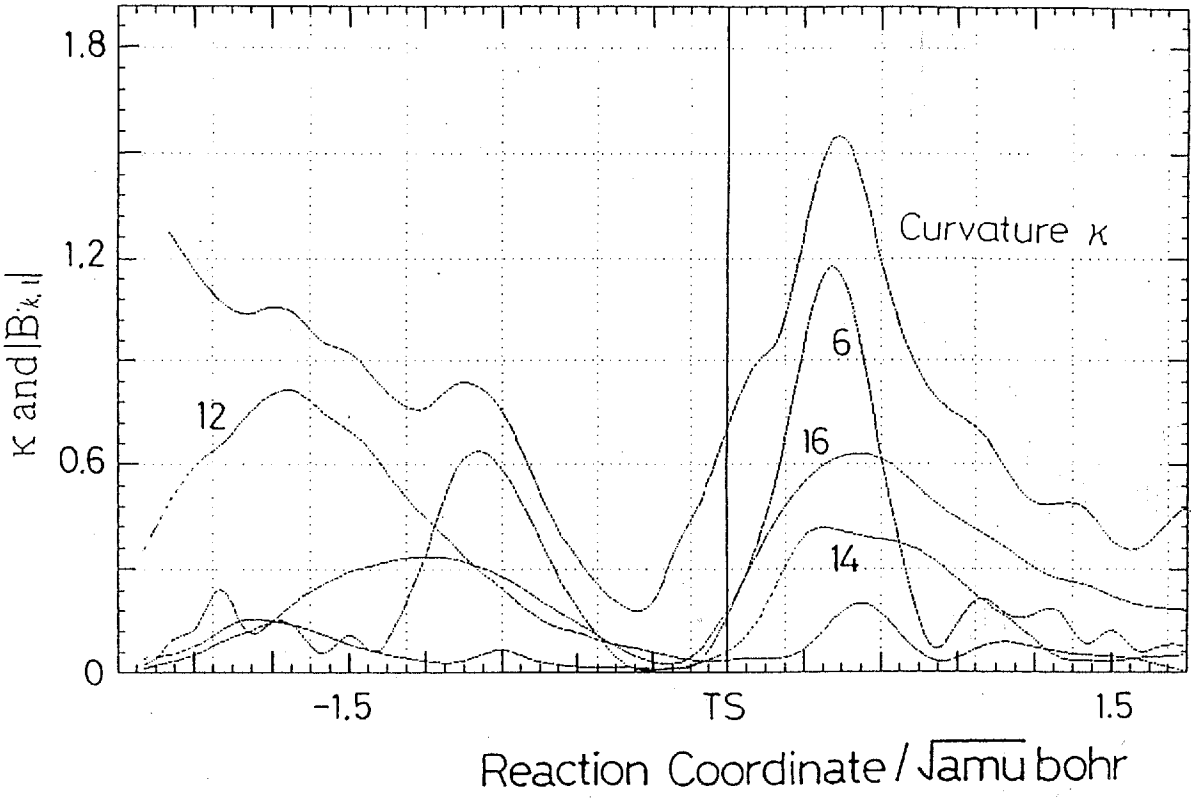

Figure 4.4: Curvature of IRC and some of its coupling elements as functions of the reaction coordinate s for the decomposition of acetaldoximé. The number k represents the mode Q_k.

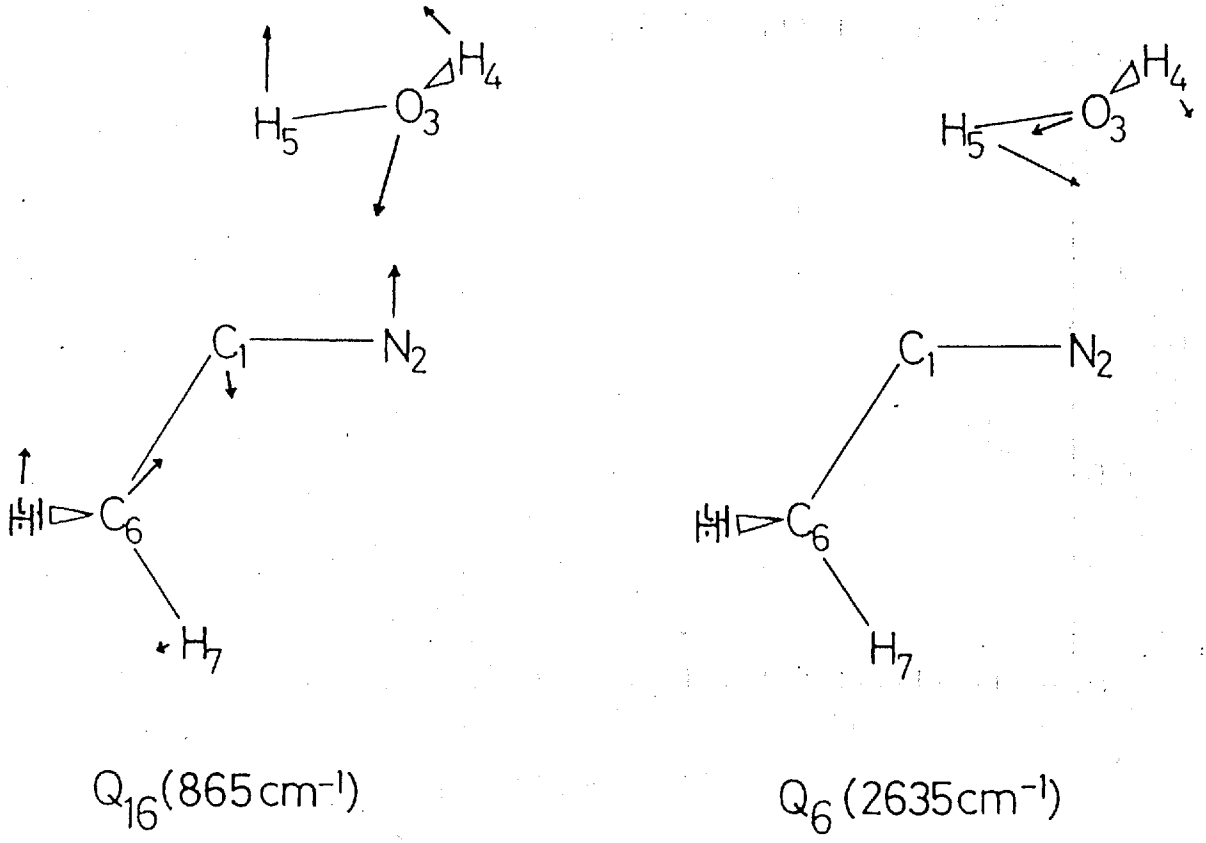

Figure 4.5: Transverse vibrational modes at $s = 0.40$ for the decomposition of acetaldoxime.

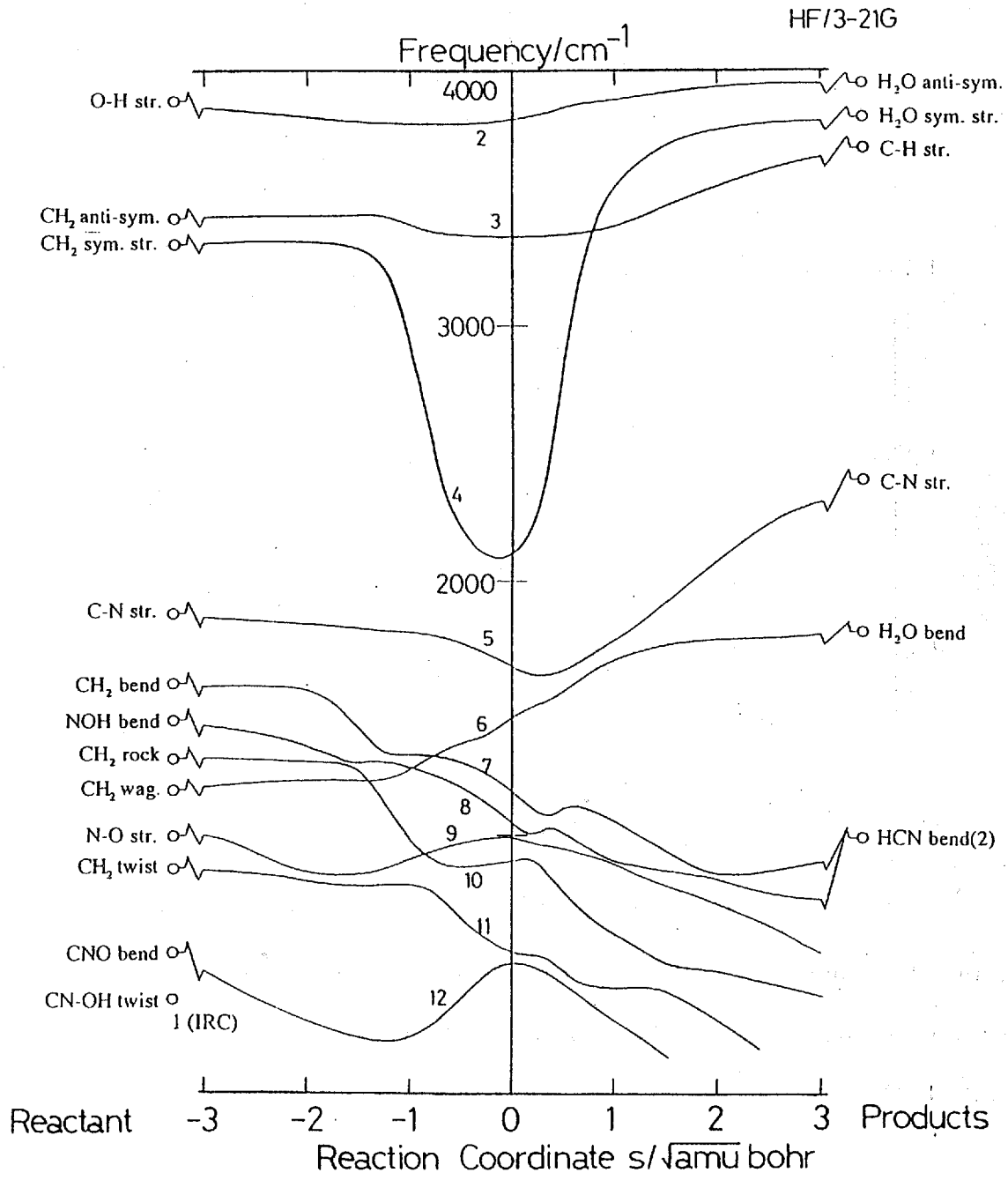

Figure 4.6: Variation of the projected frequencies along the IRC for the decomposition of formaldoxime.

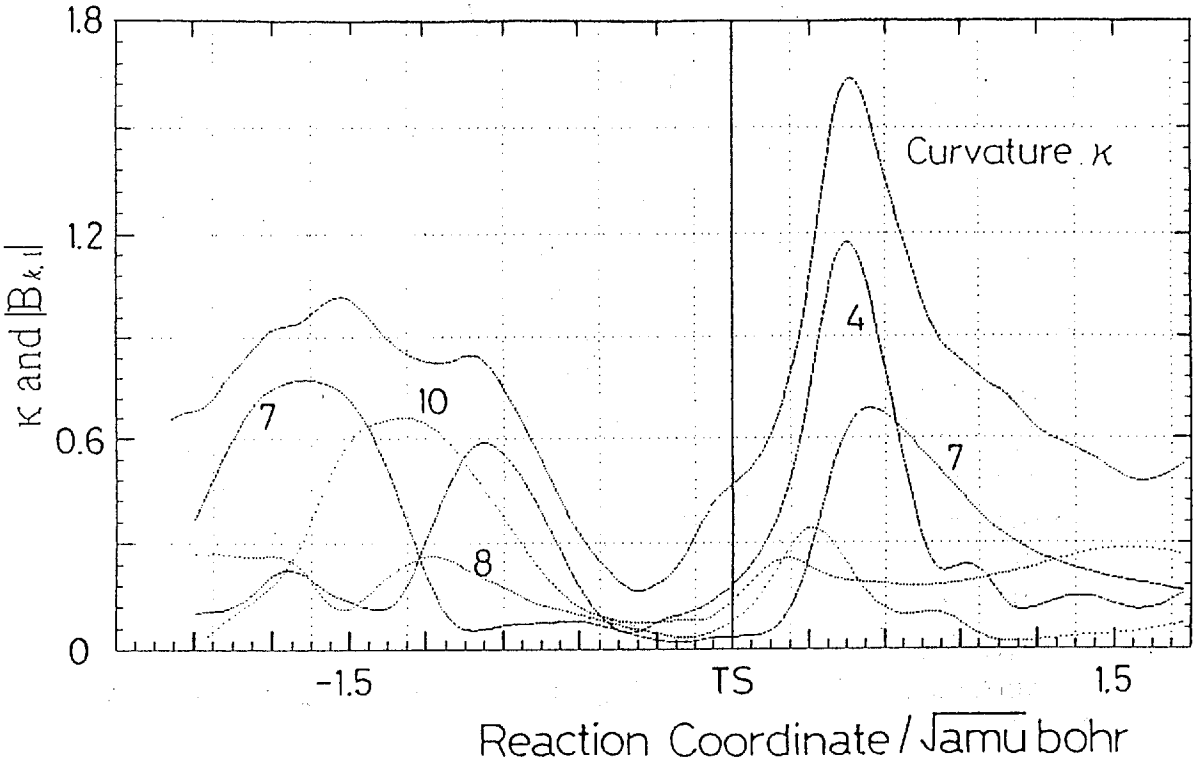

Figure 4.7: Curvature of IRC and some of its coupling elements as a function of the reaction coordinate s for the decomposition of formaldoxime. The number k represents the mode Q_k.

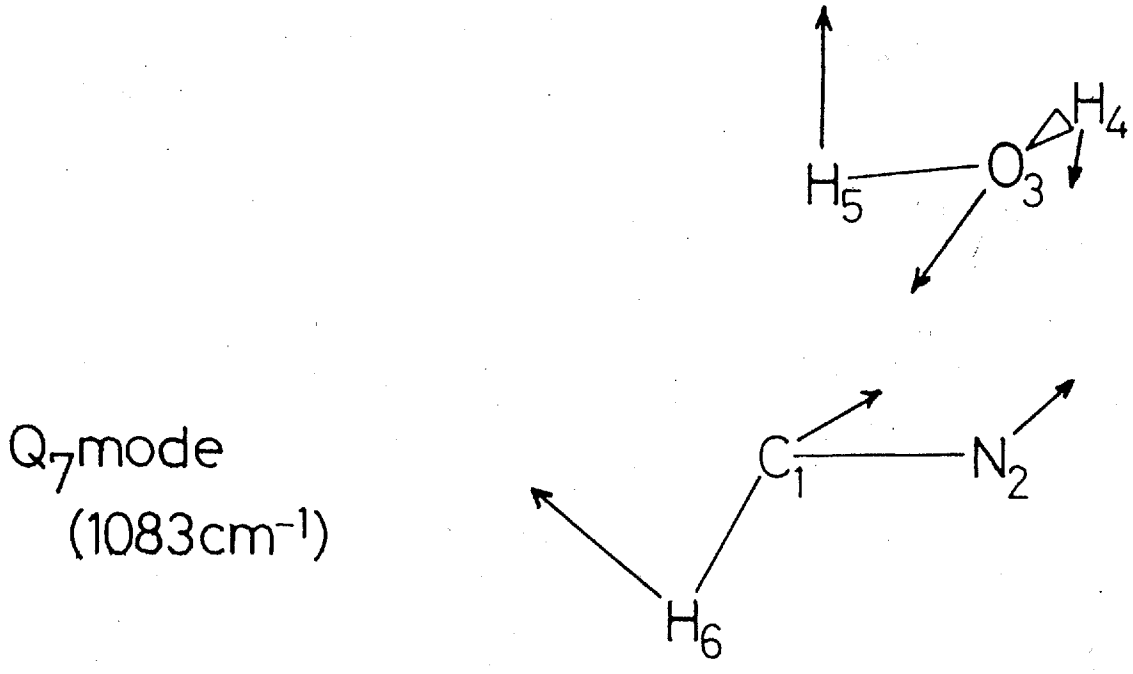

Figure 4.8: Transverse vibrational mode 7 at $s = 0.40$ for the decomposition of formaldoxime.

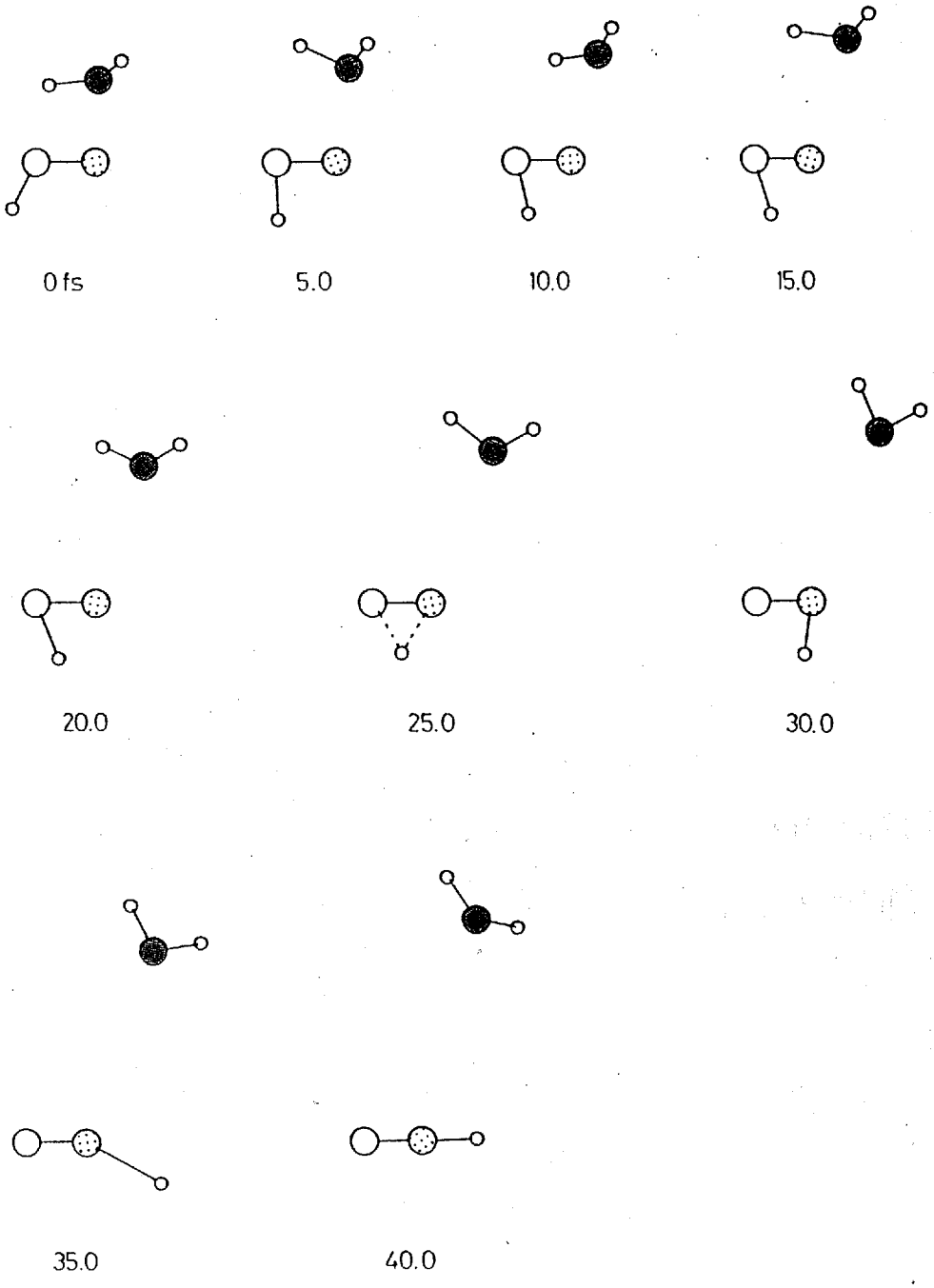

Figure 4.9: Geometries at different times for the trajectory calculation, initiating at $s = 0.40$ with an initial kinetic energy of 100 kcal/mol in the direction of mode 7 for the decomposition of formaldoxime.

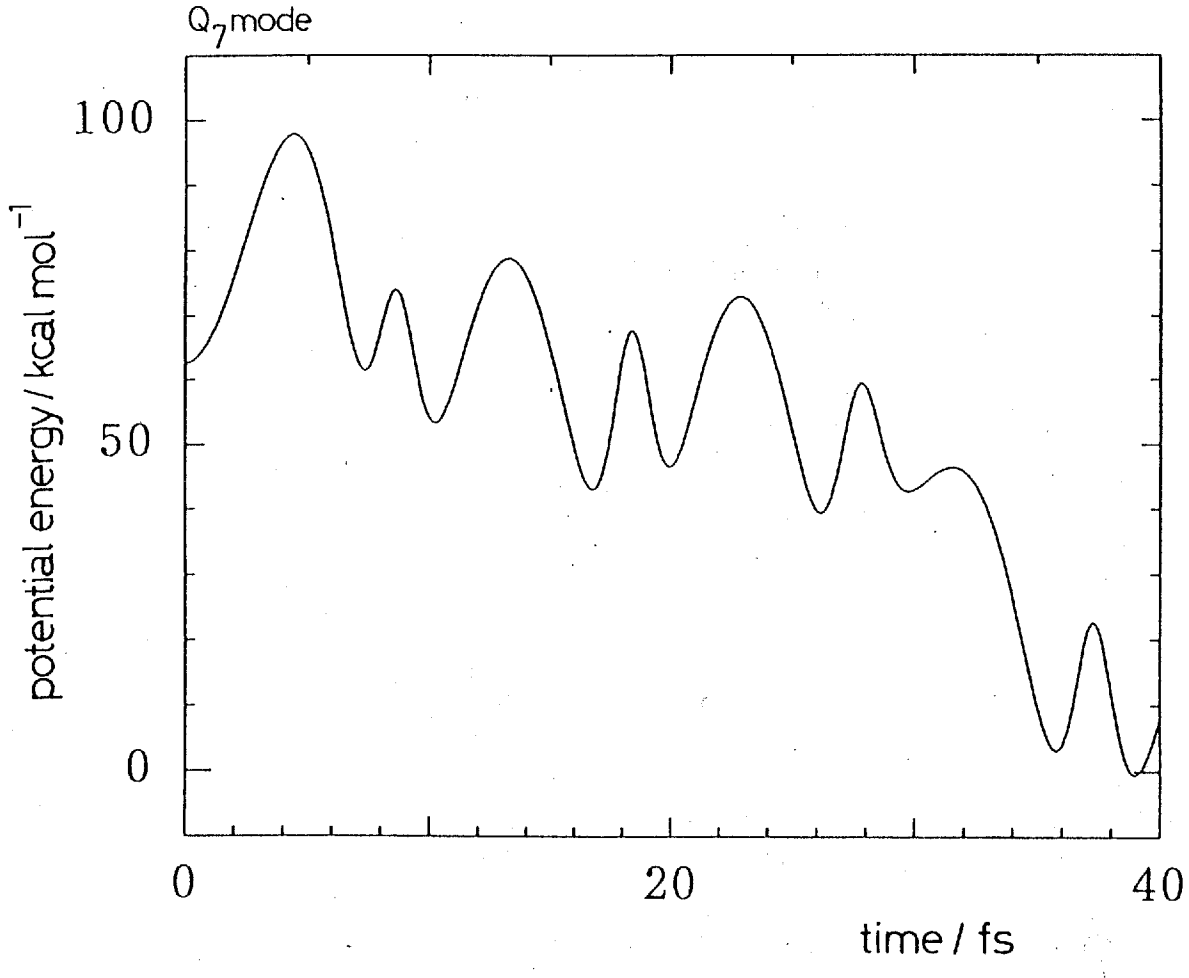

Figure 4.10: Potential energy change as a function of time from the start point of $s = 0.40$.

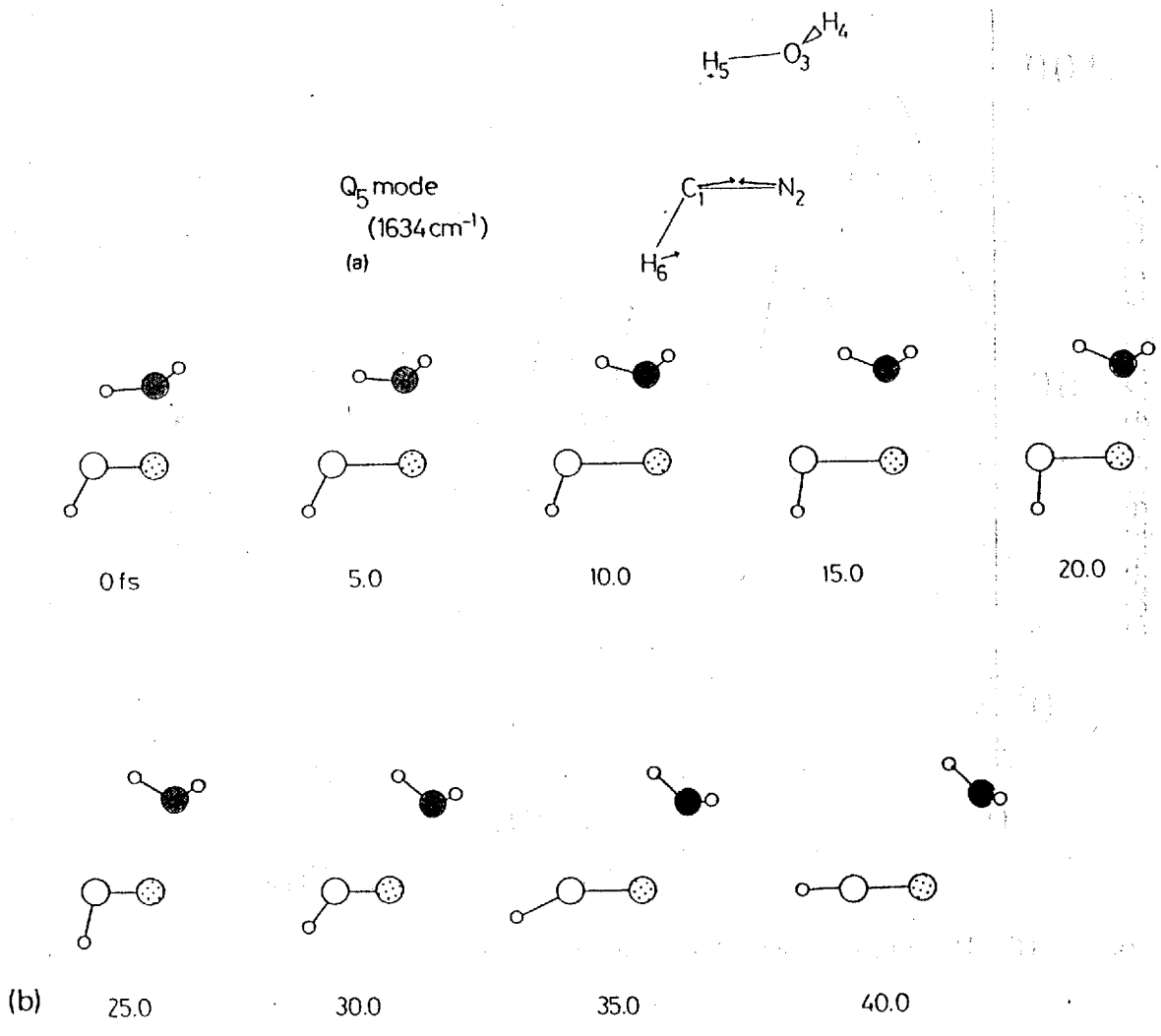

Figure 4.11: Same as (a) Figure 4.8, and (b) Figure 4.9, except for mode 5.

TABLE 4.1: Cartesian geometry (in angstrom units) and the components of mode 7

Atom	Coordinates			Mode		
	x	y	z	x	y	z
C(1)	0.	0.	0.	0.06689	0.02288	0.11046
N(2)	0.	0.	1.244930	0.07268	0.00387	0.07688
O(3)	1.703368	0.	1.318832	-0.16221	-0.00734	-0.11548
H(4)	2.088691	0.754350	1.792552	-0.27896	0.00840	-0.04661
H(5)	1.602407	0.047508	0.274899	0.59466	-0.09252	0.01456
H(6)	-0.943506	-0.028876	-0.513021	0.45247	-0.12558	-0.51859

Chapter 5

Thermal Unimolecular Reaction of Pyruvonitrile

5.1 Introduction

In this chapter, we consider pyruvonitrile as a candidate having the possibility of producing acetonitrile or methyl isocyanide during its thermal decomposition. Three reaction channels are considered for the thermal reaction of pyruvonitrile:

$$CH_3COCN \longrightarrow CO + CH_3CN(CH_3NC) \tag{5.1}$$

$$CH_3COCN \longrightarrow CH_2{=}CO + HCN \tag{5.2}$$

$$CH_3COCN \longrightarrow CH_3CONC \tag{5.3}$$

In the past, few studies reported this gas-phase reaction. Bennett et al.[58] investigated the pyrolysis at 470 °C in a flow system. They reported that the reaction proceeds via channels 5.1 and 5.2 competitively. At the present stage, however, there are no kinetic data for this reaction. Therefore, we first need to investigate the kinetics of this thermal reaction both experimentally and theoretically.

5.2 Experimental Section

The experiments were performed in a pressure-driven shock tube made of stainless steel. A schematic diagram of our experimental apparatus is shown in Figure 5.1. The apparatus and procedures used in the present study are the same as that have been described previously [59], hence only a brief description of the system is given here. The driven section is 3.67 m long with a 9.4-cm i.d. and is evacuated by a 6-in. oil-diffusion pump to less than 2×10^{-6} Torr before each run. It is separated from the driver by a polyester diaphragm. Shock waves are generated by bursting the diaphragm with a needle. Three pressure transducers are mounted flush with the inside wall 160 mm apart near the end of the driven section. Two of them are used for the measurement of the incident shock speed which is determined by counting the time intervals of shock-arrival signals with a universal counter (Takeda Riken, TR-5104G) with an accuracy of 0.1 μs. All experiments were conducted behind reflected shock waves. Reflected shock conditions for each run were calculated from the measured incident shock speed using the shock relations for the ideal gas.

A pair of MgF_2 windows is mounted on the tube walls 2 cm upstream from the end plate. The reaction is monitored by observing its vacuum-UV absorption through these windows. A microwave discharge tube containing flowing He with a few percent of additional gas is used to generate the atomic resonance light. The wavelength is selected by a monochromator (Minuteman Laboratories Inc., 302VM) and the vacuum-UV light intensity is detected by a photomultiplier (Hamamatsu, R431s). The output signals are fed into a digital storage oscilloscope and subsequently analyzed to obtain kinetic parameters. Preliminary experiments were carried out in order to find a suitable wavelength for rate analysis, and the observations at 174.4 nm were found to be appropriate for the

present reaction system. It was shown that the absorbance of the reactant is half that of the products at this wavelength. Time-resolved measurements of the reaction were also performed by using the IR emission from the product. The IR radiation is passed through a band-pass interference filter (4.90 μm) and is detected by a photoconductive HgCdTe element cooled at 77 K. The recording system is the same as in the absorption experiment.

The pyruvonitrile for the experiments was obtained commercially. After the first fraction was pumped off in a vacuum line, the sample was expanded into an evacuated glass flask, diluted with Ar (99.9995 % purity) to 0.10–0.20 mol % and stored.

For the purpose of qualitative analysis of the shock-heated gas component, the gas was taken into a glass cylinder and analyzed by gas chromatography on a 2 m Porapak-R column.

5.3 Computational Methods

Ab initio MO calculations were carried out by using the GAUSSIAN 88 [49] and GAUSSIAN 90 [50] program packages. The structures of the stationary points including transition states were fully optimized at the Hartree–Fock level by using the energy gradient technique. Vibrational frequencies were calculated at the HF/3-21G level using analytical second derivatives to correct for the zero-point energies. Finally, conventional transition-state theory [60] was used to estimate the rate constants.

5.4 Results and Discussion

5.4.1 Experimental results

The experiments were performed behind reflected shocks over the temperature range 1014–1300 K and the total density range of $(0.94\text{–}1.1)\times10^{-5}$ mol/cm^3. Time-dependent behavior was observed via both vacuum-UV absorption and IR emission during the shock heating time. Gas chromatographic analysis of the shock-heated gas revealed an absence of reaction products at temperatures < 1200 K. Decomposition products such as ketene were detected clearly above 1350 K. Thus, it seems that the time-dependent spectroscopic behavior at low temperatures in the present study, 1014–1300 K, corresponds to the following isomerization

$$CH_3CO\text{–}CN \rightleftarrows CH_3CO\text{–}NC \tag{5.4}$$

As far as we know the occurrence of reaction 5.4 has not been reported, although the MO calculations described later show that this reaction is energetically favorable. Therefore, we assume in the rate analysis that the reaction proceeds only through reaction 5.4.

Kinetic measurements were conducted by the time-resolved spectroscopic methods. Both the reactant and the product appear to have strong absorption in the vacuum-UV region. A suitable wavelength for rate analysis at 174.4 nm was found by preliminary experiments. Figure 5.2 shows a typical absorption profile at 174.4 nm for the mixture of 0.10 mol % pyruvonitrile in Ar. The absorption coefficient (base e) of the reactant is $(6.0 \pm 0.5) \times10^6$ cm^2/mol at $\sim$ 1100 K.

Evaluation of the rate constant proceeds as follows. The solution of rate equations for reaction 5.4 is [61]

$$[\mathrm{AcCN}] = \frac{[\mathrm{AcCN}]_0}{k_f + k_r}\left(k_r + k_f e^{-(k_f+k_r)t}\right)$$

$$[\mathrm{AcNC}] = \frac{k_f[\mathrm{AcCN}]_0}{k_f + k_r}\left(1 - e^{-(k_f+k_r)t}\right)$$

where k_f and k_r are the rate constants for the forward and the reverse reactions, respectively. Assuming that the Lambert–Beer law is valid over all our experimental conditions,

$$\begin{aligned}\ln\frac{I_0}{I_t} &= \varepsilon_{\mathrm{AcCN}}[\mathrm{AcCN}]l + \varepsilon_{\mathrm{AcNC}}[\mathrm{AcNC}]l \\ &= \varepsilon_{\mathrm{AcCN}}[\mathrm{AcCN}]_0 l\left\{\frac{\frac{\varepsilon_{\mathrm{AcNC}}}{\varepsilon_{\mathrm{AcCN}}}k_f + k_r}{k_f + k_r} - \frac{\left(\frac{\varepsilon_{\mathrm{AcNC}}}{\varepsilon_{\mathrm{AcCN}}} - 1\right)k_f}{k_f + k_r}e^{-(k_f+k_r)t}\right\}\end{aligned}$$

In particular at infinite time,

$$\ln\frac{I_0}{I_\infty} = [\mathrm{AcCN}]_0 l\frac{\varepsilon_{\mathrm{AcNC}}k_f + k_r}{k_f + k_r}$$

Hence

$$\begin{aligned}\varepsilon_{\mathrm{AcCN}}[\mathrm{AcCN}]_0 l\frac{\left(\frac{\varepsilon_{\mathrm{AcNC}}}{\varepsilon_{\mathrm{AcCN}}} - 1\right)k_f}{k_f + k_r}e^{-(k_f+k_r)t} &= \ln\frac{I_0}{I_\infty} - \ln\frac{I_0}{I_t} \\ -(k_f + k_r)t &= \ln\left(\ln\frac{I_0}{I_\infty} - \ln\frac{I_0}{I_t}\right) - \text{constant} \qquad (5.5)\end{aligned}$$

Thus the first-order rate constant $k_{1\mathrm{st}}$ obtained from the profile corresponds to the sum of the forward and the reverse rate constants, $k_f + k_r$. The conditions and results of our experiments are given in Table 5.1.

Kinetic measurements were also performed in the IR region. Figure 5.3 shows a typical IR emission trace at 4.90 μm. The emission intensity begins to increase with time just behind the reflected shock front. It was ascertained that the contribution of pyruvonitrile to the emission profile at this wavelength is negligible. The emission at this wavelength is mainly ascribed to isonitrile. Table 5.1 includes the results of this experiment also. Figure 5.4 displays an Arrhenius plot of $k_{1\mathrm{st}}$ values. There is no systematic change in the rate constant between these two experiments.

Evaluation of the individual rate constants requires a knowledge of the equilibrium constant K which is expressed as

$$K = \frac{k_f}{k_r} = e^{(\Delta S/R)-(\Delta H/RT)} \tag{5.6}$$

In this equation, ΔH can be obtained from the temperature dependence of the equilibrium constant. This was evaluated from our IR emission data. A least-squares fit yields the value of $\Delta H = 5$ kcal/mol, which is in excellent agreement with the calculated energy difference between pyruvonitrile and acetyl isocyanide, 5.2 kcal/mol (see Table 5.4). Using the value obtained by ab initio MO calculations, $\Delta S = 0.57$ eu, k_f and k_r were evaluated from k_{1st} and K as

$$k_f = 10^{11.49} \exp(-49.3 \text{ kcal mol}^{-1}/RT) \quad \text{s}^{-1},$$

$$k_r = 10^{11.36} \exp(-44.3 \text{ kcal mol}^{-1}/RT) \quad \text{s}^{-1}$$

5.4.2 Calculated results

There is an absence of theoretical studies on the reaction of pyruvonitrile. Unimolecular reaction paths considered are reactions 5.1 and 5.2 reported by Bennett et al.[58], and reaction 5.4 suggested by our work. The optimized geometry, total energy, and harmonic frequencies for pyruvonitrile are taken from Ref. 62. The calculated energies for some of the products were obtained from Refs. 63 and 64. Figure 5.5 shows the optimized geometries of transition states, TS1 for reaction 5.1, TS2 for reaction 5.2, and TS3 for reaction 5.4. From the full optimization, TS1 and TS2 were found to have C_s symmetry. The structure for TS3 has the nitrile group rotated by 96.2° from the carbonyl group. Cartesian coordinates of each atom of TS3 are given in Table 5.2. Each optimized geometry was confirmed to have only one imaginary vibration corresponding to motion along the reaction path. Arrows in Figure 5.5 indicate the displacement vectors along

each reaction path. The calculated frequencies for the transition states are listed in Table 5.3. Table 5.4 lists the calculated total and relative energies for the system. The lowest barrier height for reaction is found to be that for the isomerization from pyruvonitrile to acetyl isocyanide which is 58.5 kcal/mol at the HF/3-21G level, indicating that reaction 5.4 proceeds most readily. This barrier is expected to be lowered using more sophisticated methods for the MO calculation. The optimized geometry and the calculated frequencies for acetyl isocyanide are shown in Figure 5.6 and Table 5.5, respectively. No experimental spectroscopic data on acetyl isocyanide are available at the present state. However, inspection that $\nu_{\mathrm{calc}}(\mathrm{N{\equiv}C})\nu_{\mathrm{expt}}(\mathrm{C{\equiv}N})/\nu_{\mathrm{calc}}(\mathrm{C{\equiv}N}) = 2346 \cdot 2229/2588 = 2021$ cm^{-1} (4.95 μm) leads to a reasonable finding that we have monitored the IR emission from acetyl isocyanide corresponding to its NC stretching. As can be seen from Figure 5.4, the calculated $k_f + k_r$ values are seen to be in proper agreement with our experimental data of k_{1st}.

5.5 Summary

The thermal unimolecular reaction of pyruvonitrile diluted in Ar has been studied behind reflected shock waves over the temperature range 1014–1300 K, with a total density range (0.94–1.1)$\times 10^{-5}$ mol/cm^3. Acetonitrile, one of the products for reaction 5.1, was not observed in this study, contrary to the result by Bennett et al.[58] and our expectations. Instead, we now propose that the reaction proceeds by reaction 5.4 under the conditions herein. According to our calculations, unimolecular decompositions of pyruvonitrile are energetically less favorable, and the isomerization to acetyl isocyanide is dominant. Furthermore, the rate constants are consistent with those obtained experimentally. However, we obtained rate constants with the pre-exponential factors somewhat

low, which we can be ascribed to the fact that at higher temperatures decomposition to ketene from pyruvonitrile or acetyl isocyanide affects the rate analysis to some extent.

Recently, a theoretical study on the unimolecular reactions of formyl cyanide has been presented by Fang et al.[65]. They considered possible reaction channels and showed that the potential barrier for the isomerization to formyl isocyanide is lowest and that, at high temperatures, the successive decomposition proceeds with two direct molecular eliminations. Their findings are similar to our results. (More recently, the results by Fang et al. have been refined by Chang and Yu [66].)

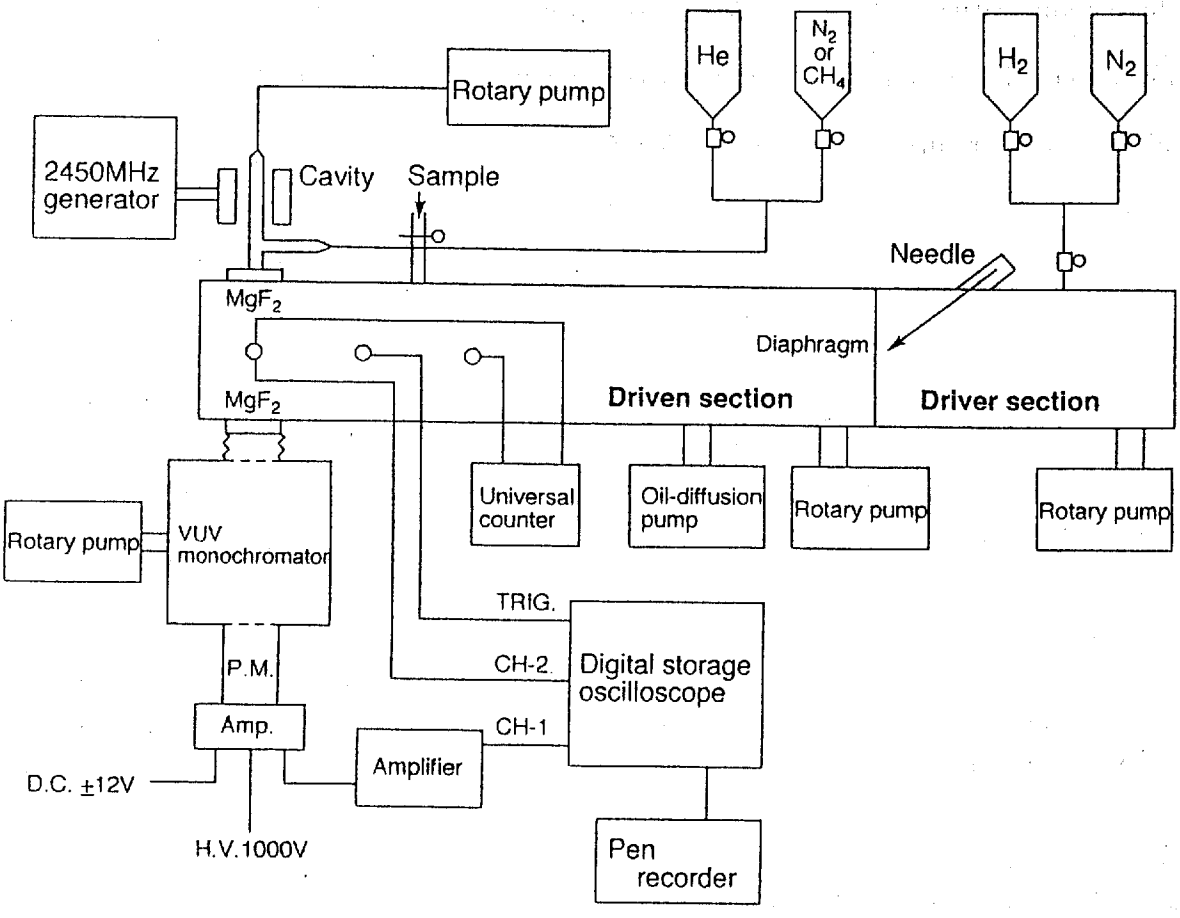

Figure 5.1: Schematic diagram of the apparatus.

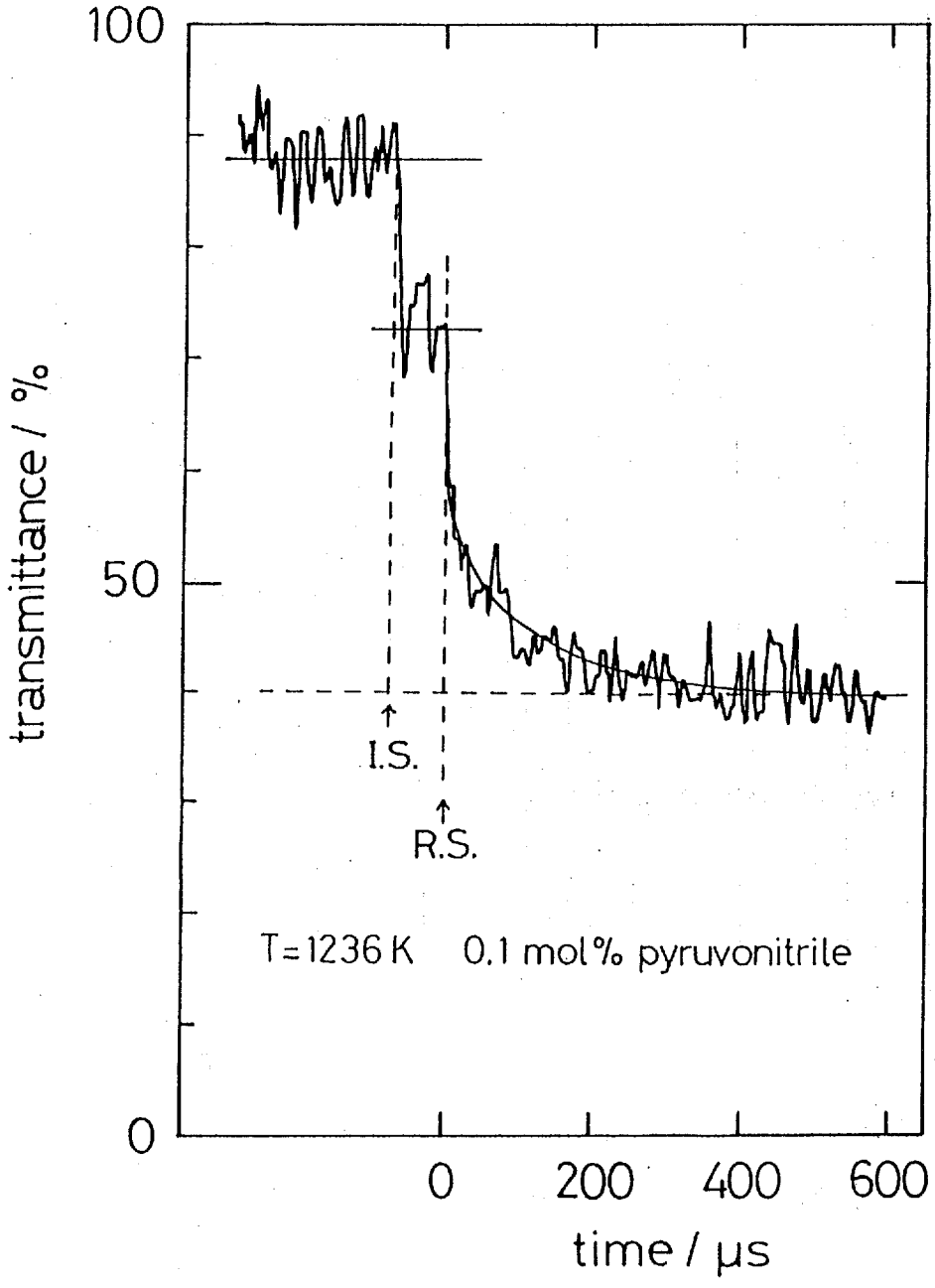

Figure 5.2: A typical absorption profile at 174.4 nm. Conditions: $T_5 = 1236$ K, $\rho_5 = 1.090 \times 10^{-5}$ mol/cm^3, 0.10 mol % reactant in Ar. IS and RS indicate the incident and the reflected shock fronts, respectively.

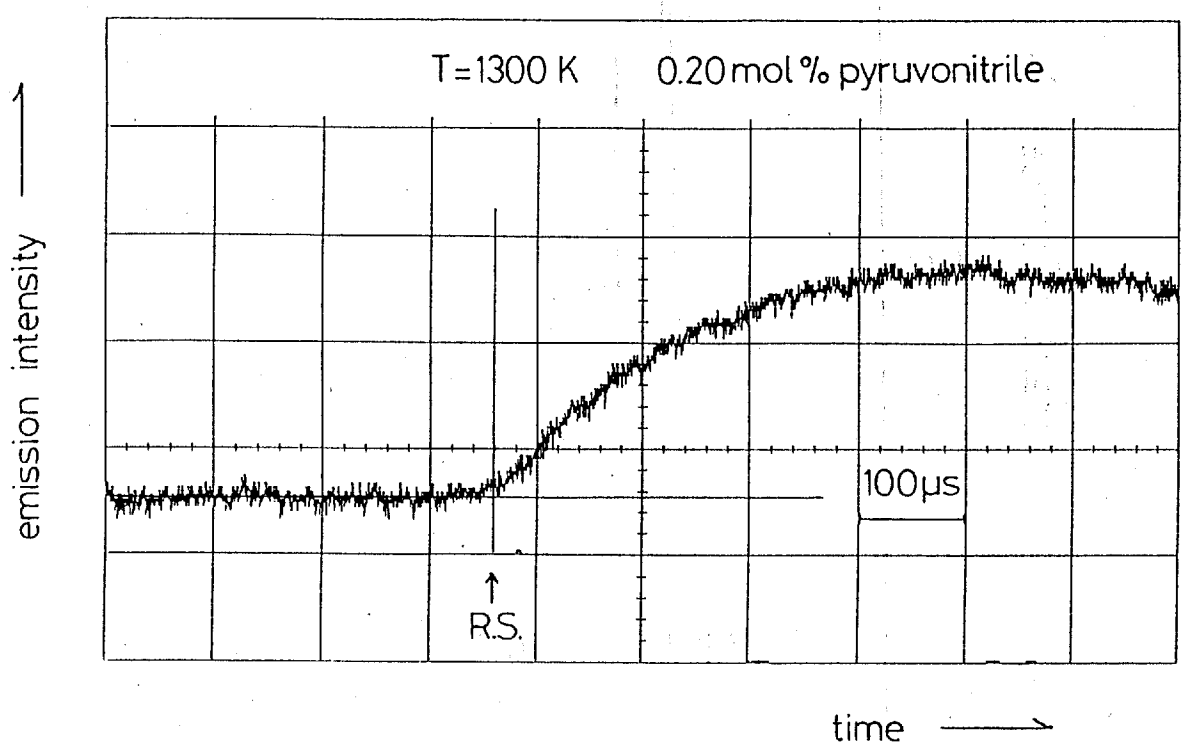

Figure 5.3: A typical emission profile at 4.90 μm. RS indicates the reflected shock front. Conditions: $T_5 = 1300$ K, $\rho_5 = 1.107 \times 10^{-5}$ mol/cm^3, 0.20 mol % reactant in Ar.

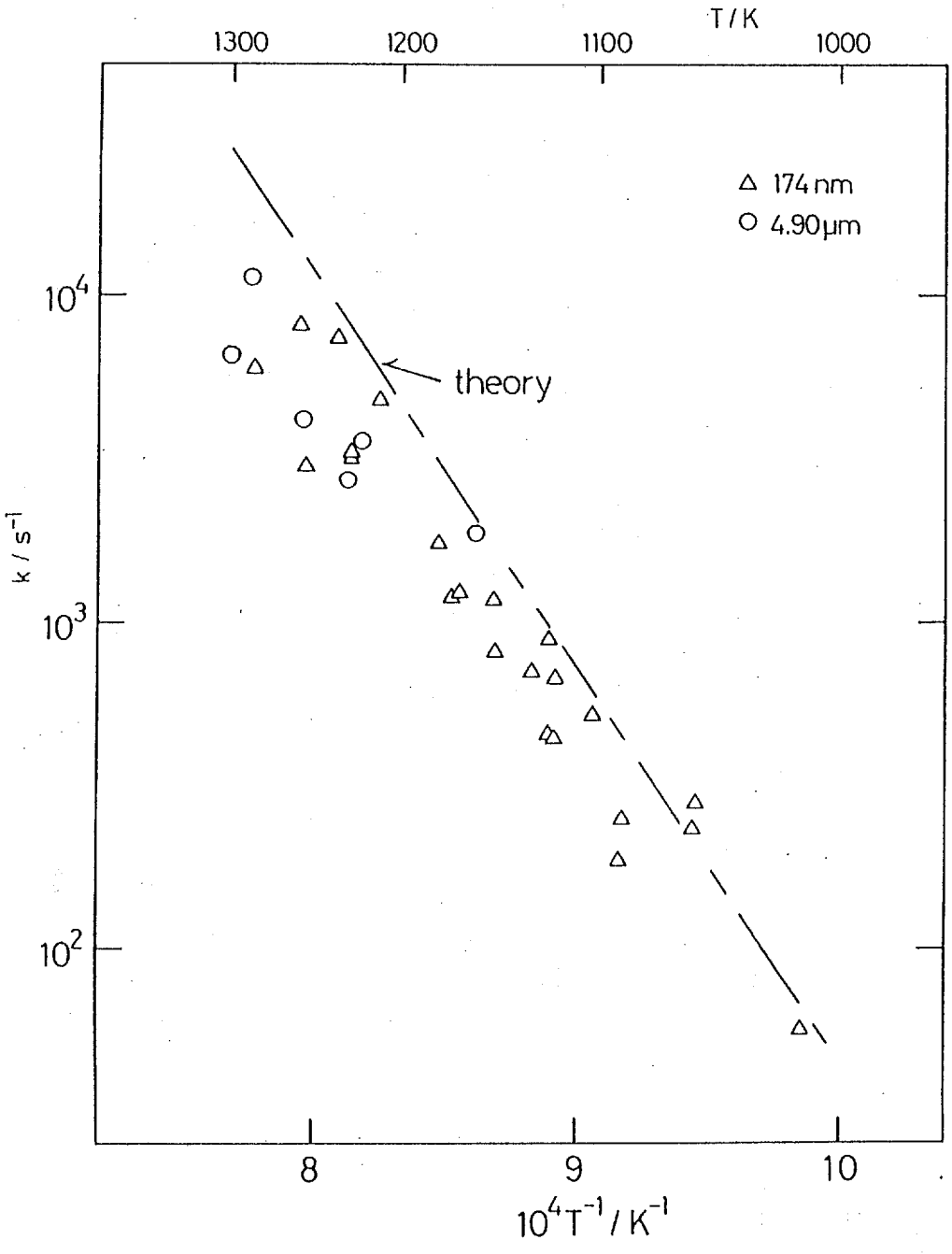

Figure 5.4: Arrhenius plot of k_{1st} and theoretical values of $k_f + k_r$.

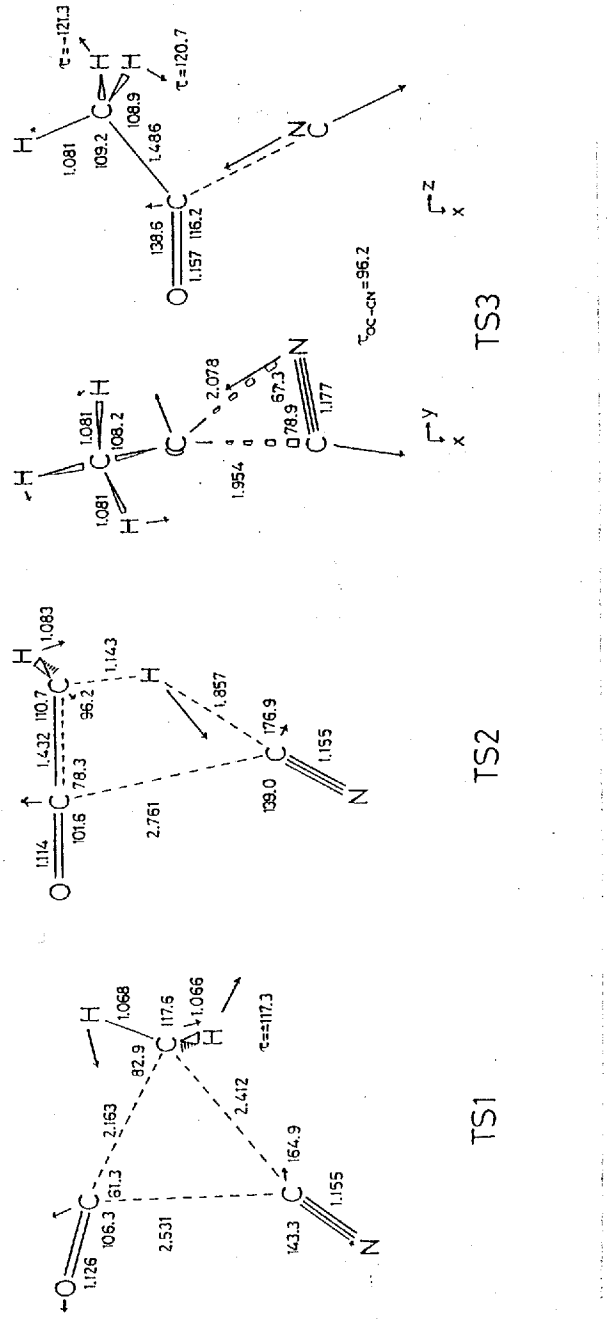

Figure 5.5: HF/3-21G optimized geometries and displacement vectors of normal mode with an imaginary frequency for transition states. Bond distances are in angstroms. Cartesian coordinates of TS3 are given in Table 5.2.

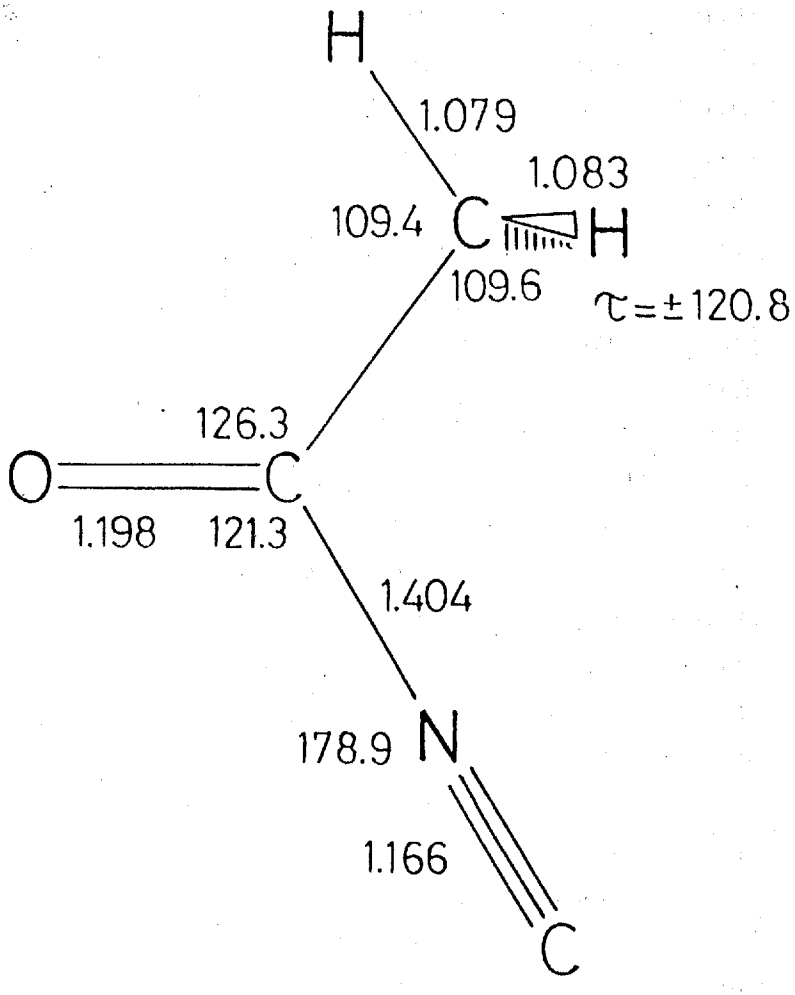

Figure 5.6: HF/3-21G optimized geometry of acetyl isocyanide. Bond distances are in angstroms.

TABLE 5.1: Rate Data for the Pyruvonitrile Reaction

P_1/Torr	M_s	$10^5\rho_5{}^a$/(mol/cm^3)	$T_5{}^a$/K	k_{1st}/s^{-1}
0.10 mol % pyruvonitrile in Ar (174 nm)				
40.1	2.079	0.9925	1091	1.88×10^2
40.6	2.254	1.113	1258	8.17×10^3
40.0	2.237	1.090	1236	7.43×10^3
39.0	2.208	1.044	1212	4.91×10^3
40.0	2.274	1.100	1286	6.03×10^3
40.5	2.179	1.070	1179	1.79×10^3
40.0	2.054	0.9850	1057	2.81×10^2
40.0	2.117	1.017	1123	4.58×10^2
40.0	2.110	1.009	1121	4.37×10^2
39.2	2.126	0.9851	1151	1.17×10^3
40.0	2.109	1.005	1123	8.90×10^2
39.8	2.034	0.9492	1058	2.32×10^2
40.0	2.221	1.074	1229	3.27×10^3
40.0	2.162	1.038	1172	1.20×10^3
40.0	1.999	0.9434	1014	5.73×10^1
40.0	2.125	1.022	1131	7.06×10^2
40.0	2.121	1.026	1120	6.77×10^2
40.0	2.239	1.079	1254	3.04×10^3
40.0	2.213	1.062	1229	3.34×10^3
41.6	2.162	1.083	1169	1.23×10^3
40.0	2.129	1.011	1149	8.10×10^2
40.0	2.076	0.9752	1103	5.19×10^2
40.0	2.064	0.9705	1089	2.55×10^2
0.20 mol % pyruvonitrile in Ar (4.90 μm)				
40.0	2.135	1.011	1159	1.90×10^3
40.0	2.236	1.071	1256	4.25×10^3
40.0	2.287	1.107	1300	6.60×10^3
40.0	2.218	1.069	1230	2.77×10^3
40.0	2.223	1.083	1223	3.65×10^3
40.0	2.288	1.120	1287	1.13×10^4

[a] Quantities with the subscript 5 refer to the thermodynamic state of the gas in the reflected shock region.

TABLE 5.2: HF/3-21G Optimized Cartesian Coordinates (Å) of TS3

atom	x	y	z
O	0.0	0.0	0.0
$C_{carbonyl}$	0.0	0.0	1.157065
$C_{nitrile}$	1.752909	0.0	2.020342
C_{methyl}	-0.956504	-0.222469	2.271725
N	1.494753	1.148658	2.032018
H	-1.933048	-0.442994	1.862659
H	-0.600719	-1.042870	2.878665
H	-0.982135	0.671642	2.877900

TABLE 5.3: HF/3-21G Calculated Vibrational Frequencies (cm^{-1}) for Transition States

	TS1		TS2	TS3
a′	3491.7	a′	3240.3	3320.2
	3325.7		2543.6	3316.5
	2392.7		2398.8	3228.8
	2337.1		2336.8	2196.4
	1551.9		1564.6	2117.3
	1400.5		1407.0	1622.2
	846.1		1161.6	1617.7
	473.4		821.9	1564.7
	369.7		359.2	1207.6
	226.4		286.0	1193.5
	88.7		97.4	949.4
	742.4i		561.3i	529.0
a″	3525.3	a″	3312.6	521.3
	1599.3		1628.4	398.7
	876.0		1257.3	342.5
	255.8		506.0	217.7
	211.8		302.3	171.6
	151.2		122.6	483.0i

TABLE 5.4: Total Energies (hartrees), Zero-Point Energies (In Brackets, kcal/mol), and Relative Energies (In Parentheses, kcal/mol +ZPE[a]) Relative to Pyruvonitrile

pyruvonitrile[b]	acetonitrile	carbon monoxide[c]	hydrogen cyanide[c]	ketene[d]
-243.267908	-131.191802	-112.09330	-92.35408	-150.87653
[37.3]	[31.0]	[3.3]	[11.5]	[21.8]
(0.0)		(−13.8)	(19.4)	
acetyl isocyanide	TS1	TS2	TS3	
-243.258889	-243.079202	-243.136597	-243.171006	
[36.9]	[33.1]	[33.4]	[35.0]	
(5.2)	(114.1)	(78.4)	(58.5)	

[a] +ZPE represents the energies with zero-point energy corrections.

[b] Reference 62.

[c] Reference 63.

[d] Reference 64.

TABLE 5.5: HF/3-21G Calculated Vibrational Frequencies (cm^{-1}) of Acetyl Isocyanide

symmetry species	no.	frequency	approximate assignment
a′	1	3327.4	CH_3 antisym. str.
	2	3219.8	CH_3 sym. str.
	3	2346.1	N≡C str.
	4	1969.3	C=O str.
	5	1626.9	CH_3 antisym. bend.
	6	1570.0	CH_3 sym. bend.
	7	1287.0	C–C str.
	8	1101.6	CH_3 rock.
	9	791.5	C–N str.
	10	671.4	CCN bend.
	11	460.4	CCO bend.
	12	200.4	CNC bend.
a″	13	3277.6	CH_3 antisym. str.
	14	1644.7	CH_3 antisym. bend.
	15	1202.5	CH_3 rock.
	16	678.5	C=O wag.
	17	277.3	CNC bend.
	18	166.8	CH_3 torsion

Chapter 6

Thermal Unimolecular Decomposition of Isoxazole

6.1 Introduction

In this chapter, two reaction channels occurred in the unimolecular processes are studied by the method described in Chapter 3 for the thermal decomposition of isoxazole. Lifshitz and Wohlfeiler [67] conducted a experimental study on the thermal decomposition of isoxazole, using a single-pulse shock tube over the temperature range 850–1100 K. They reported that acetonitrile and carbon monoxide are the major decomposition products, followed by minor products such as hydrogen cyanide, acrylonitrile. They also performed experiments containing large quantities of toluene as a radical scavenger, and found that there is no effect on the production of acetonitrile and a small effect on the formation of hydrogen cyanide. They proposed the following reaction mechanism from their results. The thermal decomposition is occurred by complex reactions involving free-radical reactions, but acetonitrile and hydrogen cyanide are formed by unimolecular processes, the

latter being formed also by radical mechanism. The process to yield acetonitrile takes place by a simultaneous N–O bond cleavage, a hydrogen atom rearrangement, and the removal of carbon monoxide:

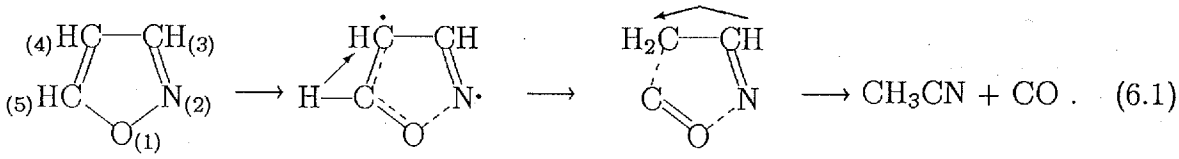

(6.1)

Hydrogen cyanide and ketene can be directly formed by a unimolecular cleavage of the ring, as follows:

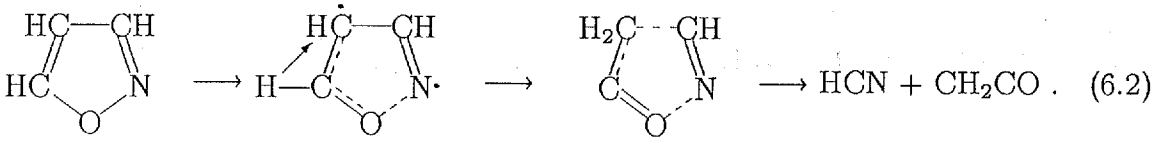

(6.2)

These two processes constitute the competitive reaction in which the pathway to the formation of an intermediate is the same, and the process 6.1 is the main channel. It is interesting to investigate theoretically why the reacting molecule prefers the channel 6.1. To the best of our knowledge, there is no theoretical study on the decomposition of isoxazole. Thus, in the present work we study this reaction system by means of ab initio MO calculations, with particular attention to the dynamical features of the reaction. As the construction of a complete potential energy surface would be practically impossible, we analyze a minimum energy path to get detailed information about the dynamics.

6.2 Results and Discussion

6.2.1 Stationary points

The optimized geometrical parameters of the reactant isoxazole are given in Table 6.1 together with the experimental data [68]. The parameters obtained with HF/4-31G

by Komornicki et al.[69] are also included for comparison. It follows from Table 6.1 that the calculated bond angles agree well with the experimental counterparts to within 1.3°. As for the bond lengths, HF/6-31G** method predicts a slightly small ring structure. The maximum difference arises in N–O bond length for both 3-21G and 6-31G** basis sets; the former level predicts larger than the experimental value while smaller value was obtained at the 6-31G** level. Table 6.2 lists the experimental and calculated vibrational frequencies of isoxazole. The calculated frequencies show small systematic deviations from the experimental data [70], as is generally the case [71]. Exception is for mode ν_9 with the 3-21G basis set, being in good agreement with experiment.

Other stationary points on the reactive system are given in Figure 6.1. The structure labeled TS-1 is the transition structure to form an intermediate (INT) from isoxazole. The normal mode corresponding to the imaginary frequency consists primarily of the transfer of an H atom, as denoted by the arrows in Figure 6.1. Note that the planarity in the ring structure is broken in TS-1, where an N–O bond length is almost the same as that of isoxazole as was mentioned by Lifshitz and Wohlfeiler [67]. In INT is recovered the planarity of the ring.

The process 6.2 is completed if the formed intermediate successively reacts by rupturing an N–O bond and a C–C bond in the positions 3 and 4. This transition state is shown as TS-2 in Figure 6.1. This gives a planar ring structure with C_s symmetry. The stretch of the N–O bond is much larger than that of the breaking C–C bond, reflecting the difference in the bond strength.

When another C–C bond (positions 4 and 5) is ruptured together with a hydrogen atom transfer, acetonitrile and carbon monoxide are produced according to the scheme 6.1. Note again that Lifshitz and Wohlfeiler reported this reaction as the main decomposition channel. The optimization of the transition state resulted in a structure depicted as TS-3

in Figure 6.1. However, the IRC calculation revealed that TS-3 corresponds to the saddle point for the reaction

$$HCN + CH_2CO \longrightarrow CH_3CN + CO\ . \tag{6.3}$$

Hence, no transition state could be found for the direct formation of acetonitrile and carbon monoxide from isoxazole. Therefore, we obtained in the calculations TS-3 for reaction 6.3 and following two transition states for the reaction

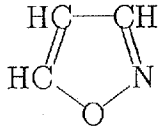

$$\longrightarrow \text{TS-1} \longrightarrow \text{INT} \longrightarrow \text{TS-2} \longrightarrow HCN + CH_2CO\ . \tag{6.2'}$$

The calculated total and relative energies are summarized in Table 6.3. It follows that improvement of the basis set lowers the reaction barriers. Nevertheless, the potential barrier at the first step is high, thus the experimental results (52 kcal/mol) could be interpreted by the consequence of a large amount of energy transfers in the system to stray from the steepest-descent path. The dynamical energy transfers can be analyzed with respect to the nuclear motion along the IRC and transverse vibrational motions, based on the reaction-path Hamiltonian approach [39,40]. The first treatments for the unimolecular elimination reactions are found in Ref. 55 .

6.2.2 IRC analysis

In order to investigate the dynamical features of the reaction, we traced the IRC at the first step which connects reactant and intermediate. Figure 6.2a shows the potential energy profile along the IRC together with geometrical changes. Zero-point vibrational energies are not included in obtaining the energy profile. It can be seen that the five-membered ring has a non-planar structure at any points along the IRC, except at reactant and at intermediate.

The variation of the frequencies along the IRC is plotted in Figure 6.3. On connecting these points, we adopted the following criteria of crossing or noncrossing: two points which are similar in the displacement vectors are connected, and the discontinuous change should not occur in the vibrational modes. Therefore, our treatment corresponds to the one based on the "diabatic" or "nonadiabatic" representation of vibrational modes [56]. It should be noted that the mode representing the reaction path does not appear because it has been projected out. The reaction path mode corresponds to the normal mode of the lowest frequency at stable stationary points. The frequency for mode Q_4 (ν_2 at reactant) changes substantially because this mode is related to the motion of the C–H bond to be broken.

The nonadiabatic couplings of vibrational modes due to the curvature of the IRC are represented by the coupling elements $B_{k,1}(s)$, which cause the energy transfer from the curving of the IRC to the particular generalized normal modes. The correlation with the vibrational modes of lower frequencies plays an important role in the course of the reaction. Figure 6.2b displays the selected coupling elements for such modes that change appreciably and curvature κ as a function of the reaction coordinate. It can be seen that κ becomes extremely large near the intermediate, where the vibrational mode that couples strongly to the IRC is Q_{17}. Figure 6.4 displays this local mode at $s = 2.30\ \sqrt{\text{amu}}$ bohr where the coupling element $B_{17,1}$ has a peak. Gradient vector at this point is also shown in the figure. This mode posesses a component of CO elimination as well as that of the H atom rearrangement. It is therefore anticipated that the process 6.1 occurs by a large amount of energy supply from the IRC to this mode. We then carried out trajectory calculations starting from this point and monitored how it goes.

6.2.3 Classical trajectory calculations

To demonstrate the effect of dynamical features on the reaction path selectivity, we performed the classical trajectory calculations. Trajectories were initiated at $s = 2.30$ $\sqrt{\text{amu}}$ bohr with an initial internal velocity vector in the direction of mode Q_{17}, and the successive elimination process was traced. The initial geometry and the components of mode Q_{17} are given in Figure 6.4. The decomposition to yield carbon monoxide occurred when an initial kinetic energy of 70 kcal/mol or more was given to this mode. Figure 6.5 illustrates the geometrical changes of the system with time. In this rather oversimplified simulation reacting molecule decomposed to vinyl nitrene, but acetonitrile was not produced. However, it has been reported [72] that vinyl nitrene undergoes isomerization to acetonitrile with very low activation energy, thus the isomerization appears to proceed easily also in this reaction. It should be noted that in the real system reacting molecule does not actually require this much of kinetic energy, since this calculation is the first approximation for elucidating the mode specificity of the reaction, in addition to the moderate basis set being employed.

For the purpose of comparison, another run of trajectory calculation was carried out. Initial conditions were the same as that described above, except for starting from the intermediate. The result of this run is given in Figure 6.6. In strong contrast to the result shown in Figure 6.5, decomposition to hydrogen cyanide and ketene took place. The results convincingly demonstrate that a particular geometry and a specific vibrational mode during the course of the reaction play a critical role in controlling the consecutive reaction channel.

6.3 Summary

Two reaction channels occurred in the unimolecular processes were studied by ab initio MO calculations for the thermal decomposition of isoxazole. These paths constitute the competitive reaction branching from the reaction intermediate. However, MO calculations did not show any transition state for the reaction route to produce acetonitrile and carbon monoxide, although in the experiment these were found as the major products. We considered that this reaction channel was opened by a dynamical effect due to the mode couplings between the reaction path and vibrational modes. We have investigated this effect in the reaction theoretically employing the combined approach of the IRC and classical trajectory calculations.

The IRC calculation indicates that a large curvature of the reaction path exists near the reaction intermediate, and that a particular local vibrational mode Q_{17} which couples strongly to the IRC plays a critical role in controlling the consecutive decomposition channel. That is, a bifurcation occurs just before the intermediate to produce acetonitrile and carbon monoxide. Classical trajectory calculations proved these findings, which is in conformity with the experimental results.

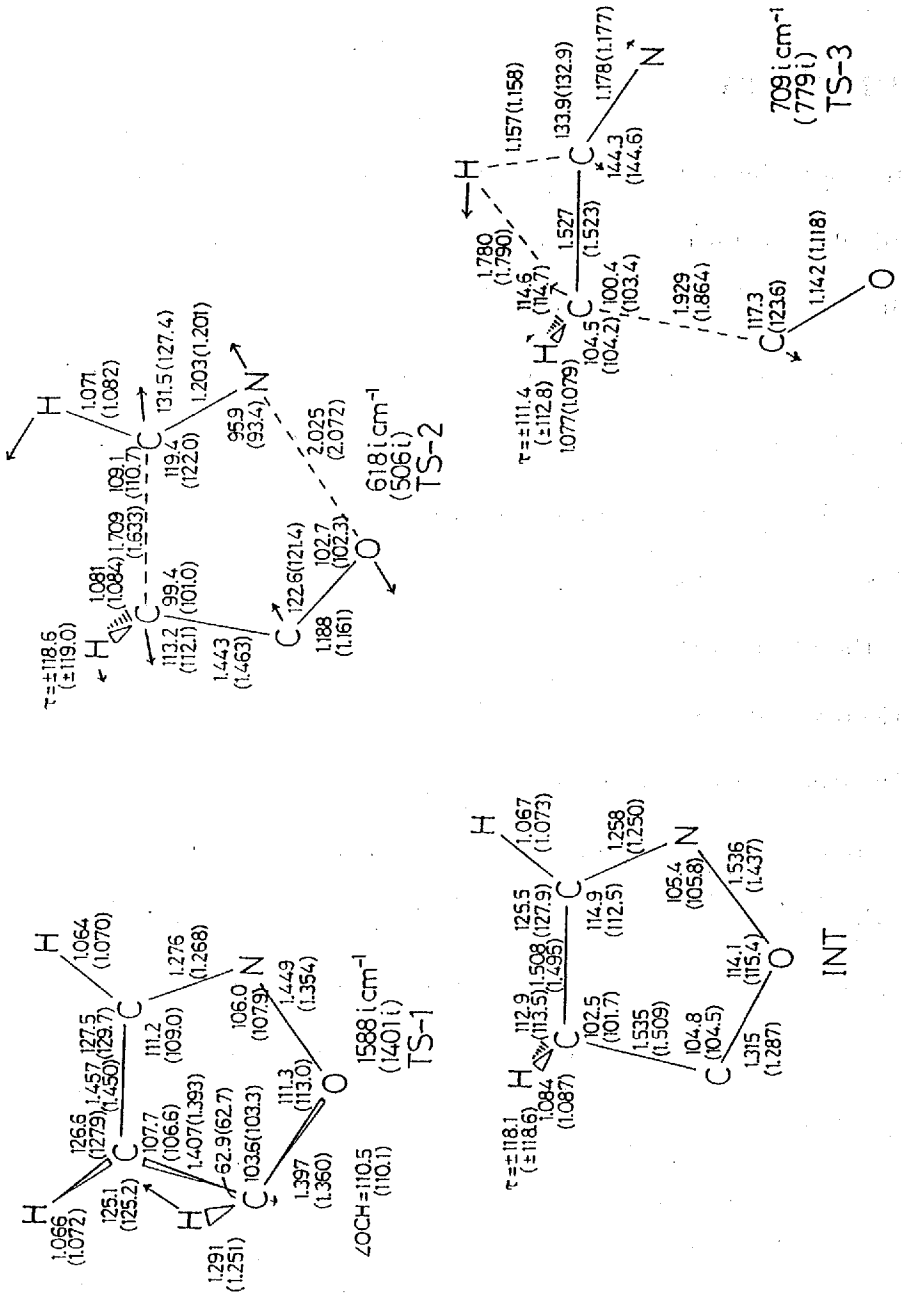

Figure 6.1: HF/3-21G and HF/6-31G** optimized geometries (angstroms and degrees) for the various species in the reaction paths. Values in parentheses indicate the parameters with the 6-31G** basis set.

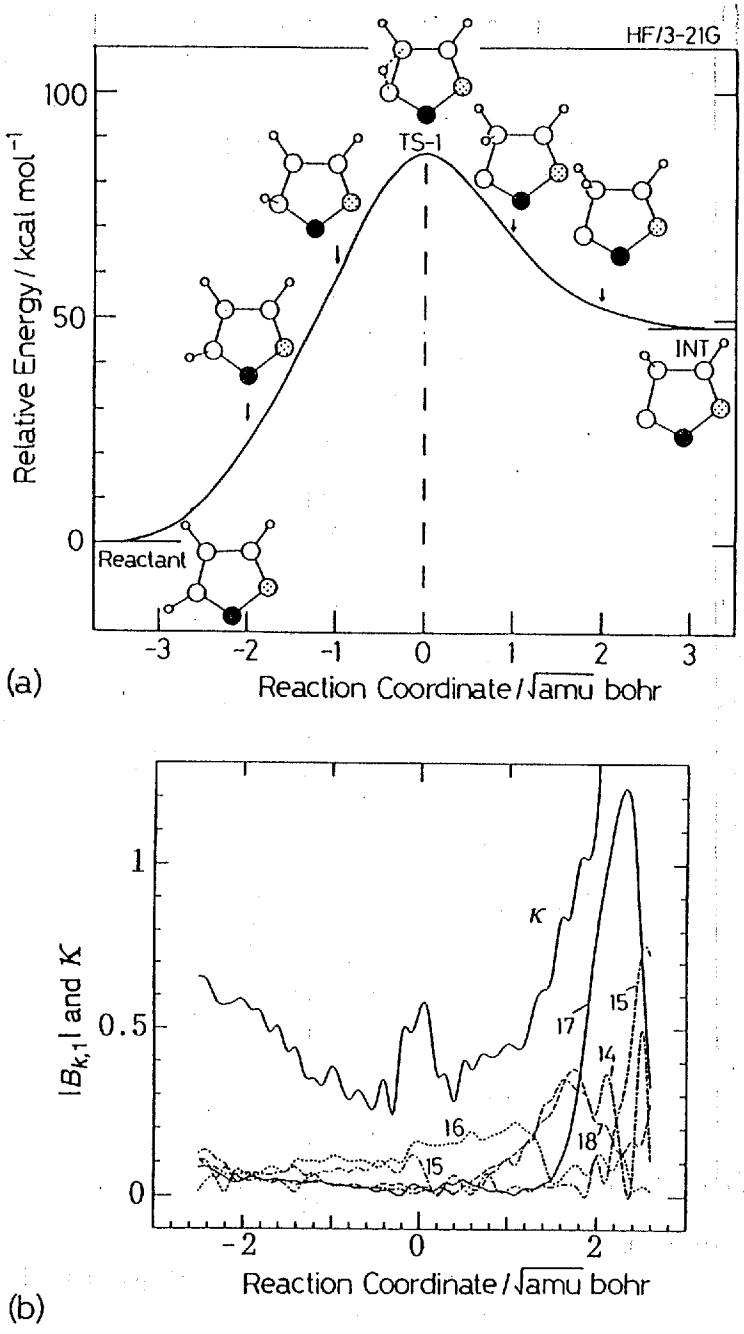

Figure 6.2: (a) HF/3-21G potential energy profile and geometrical changes along the IRC, and (b) curvature and the selected coupling elements along the IRC.

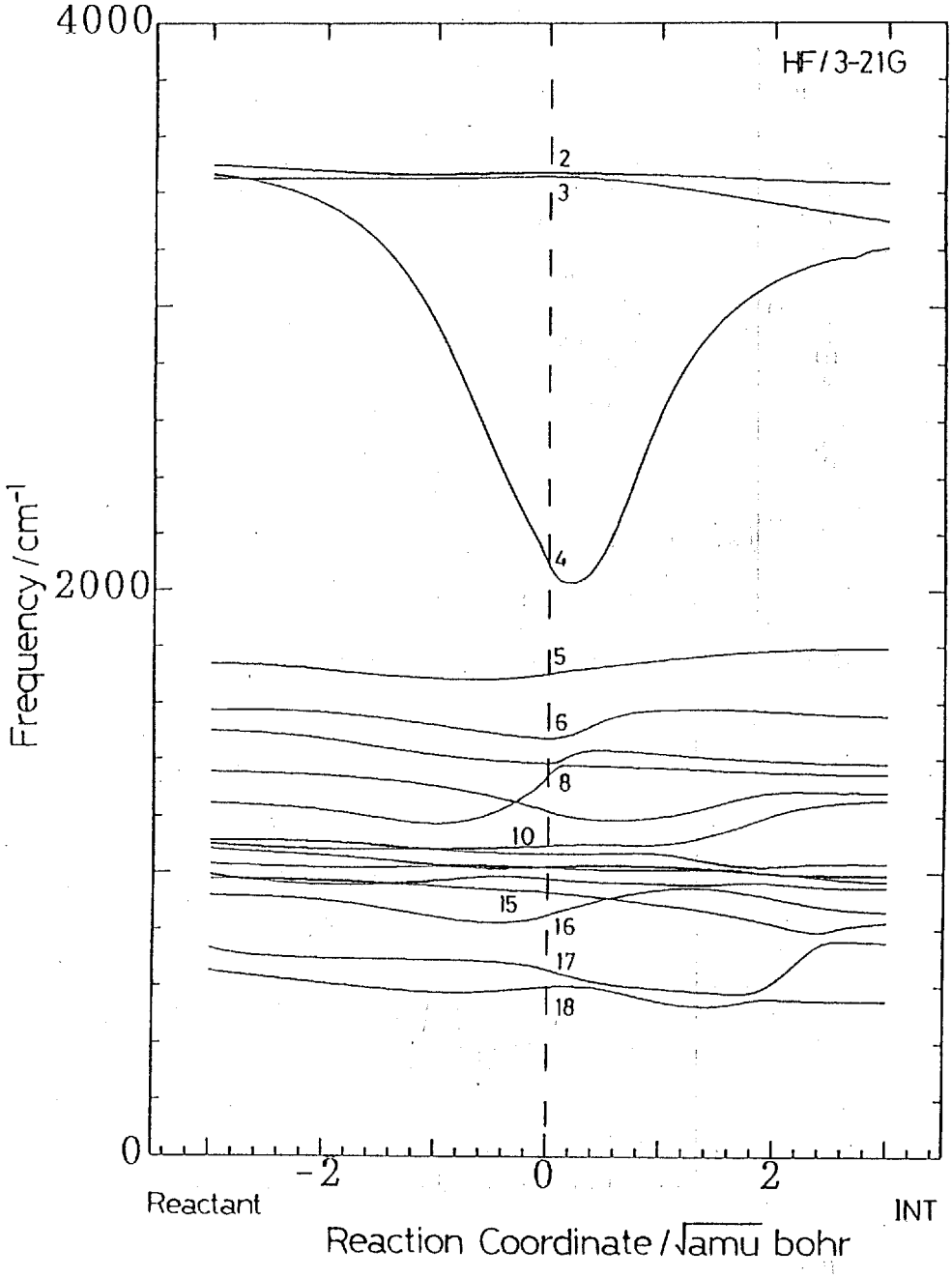

Figure 6.3: Changes of the generalized vibrational frequencies along the IRC. The modes are labeled as appropriate for the saddle point.

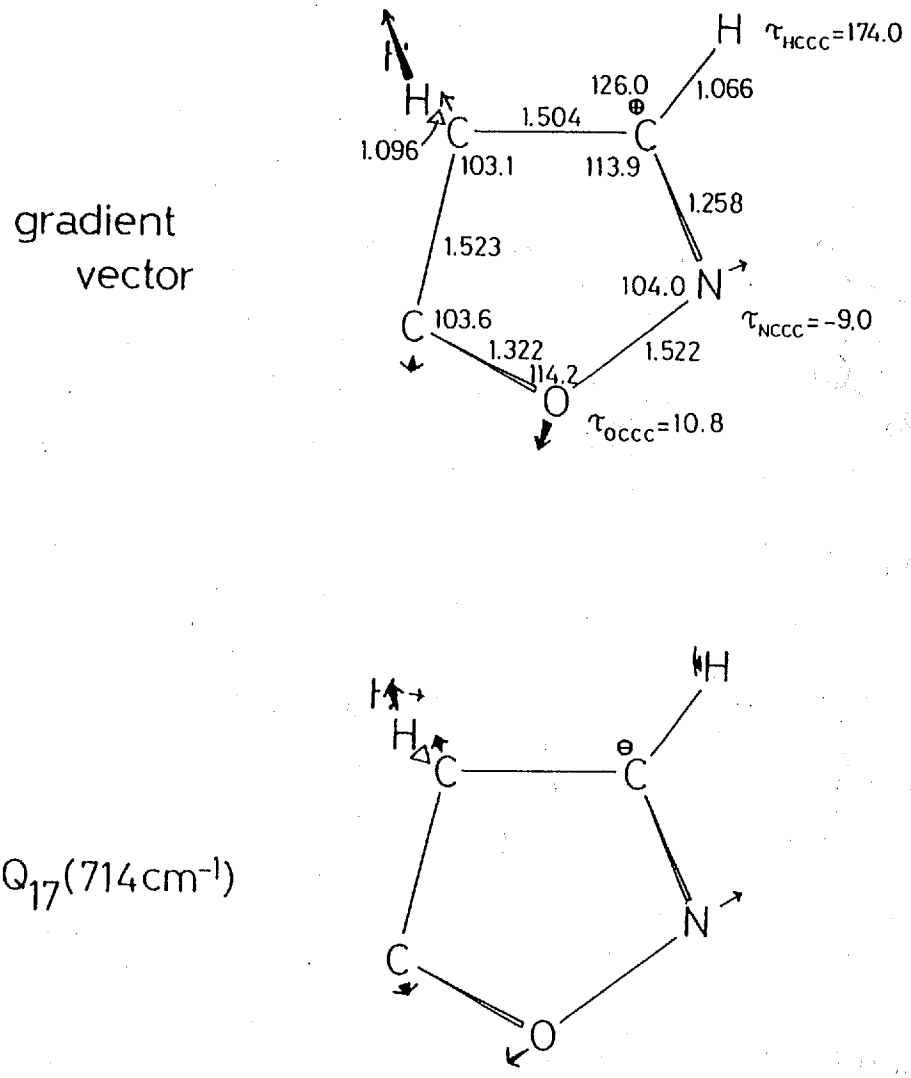

Figure 6.4: Selected geometry parameters (angstroms and degrees), gradient vector, and transverse vibrational mode Q_{17} at $s = 2.30$ $\sqrt{\text{amu}}$ bohr.

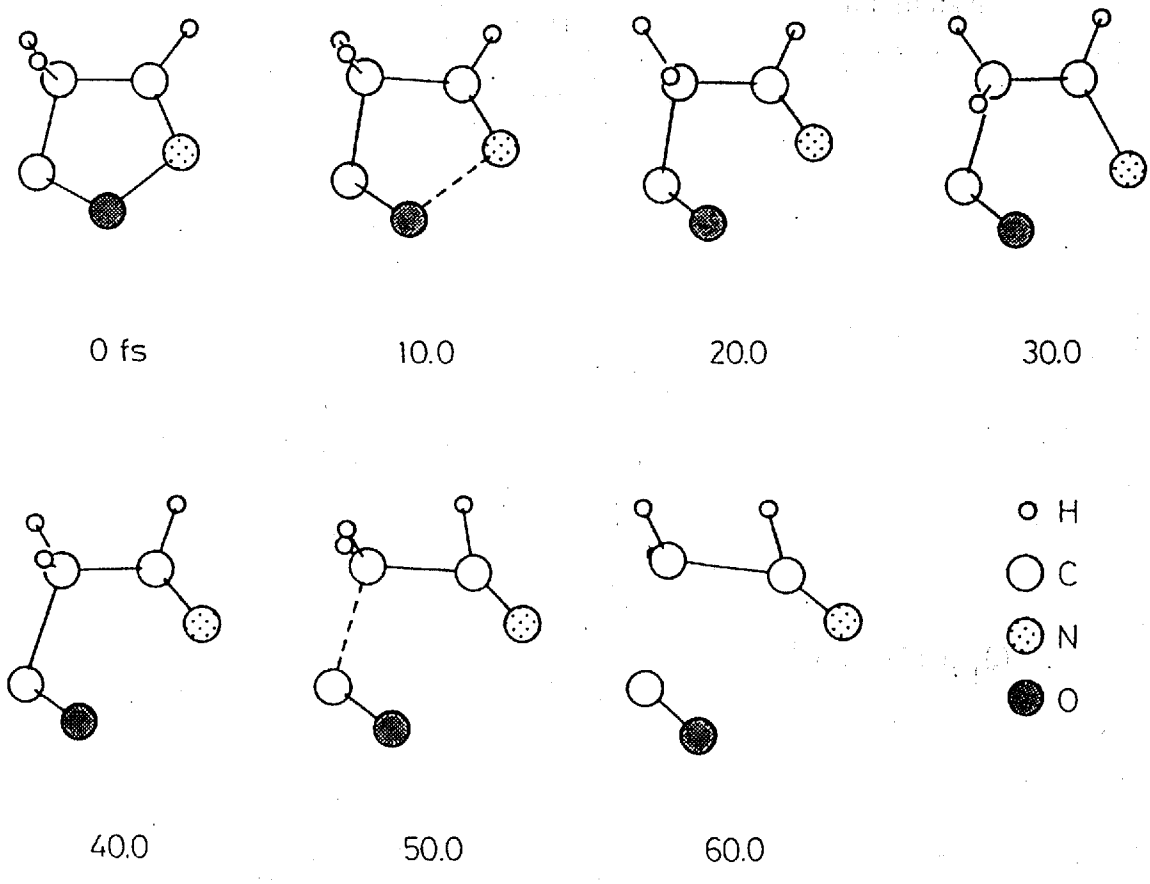

Figure 6.5: Geometries at different times for the trajectory calculation, initiating at $s = 2.30\ \sqrt{\text{amu}}$ bohr with an initial kinetic energy of 70 kcal/mol in the direction of Q_{17}.

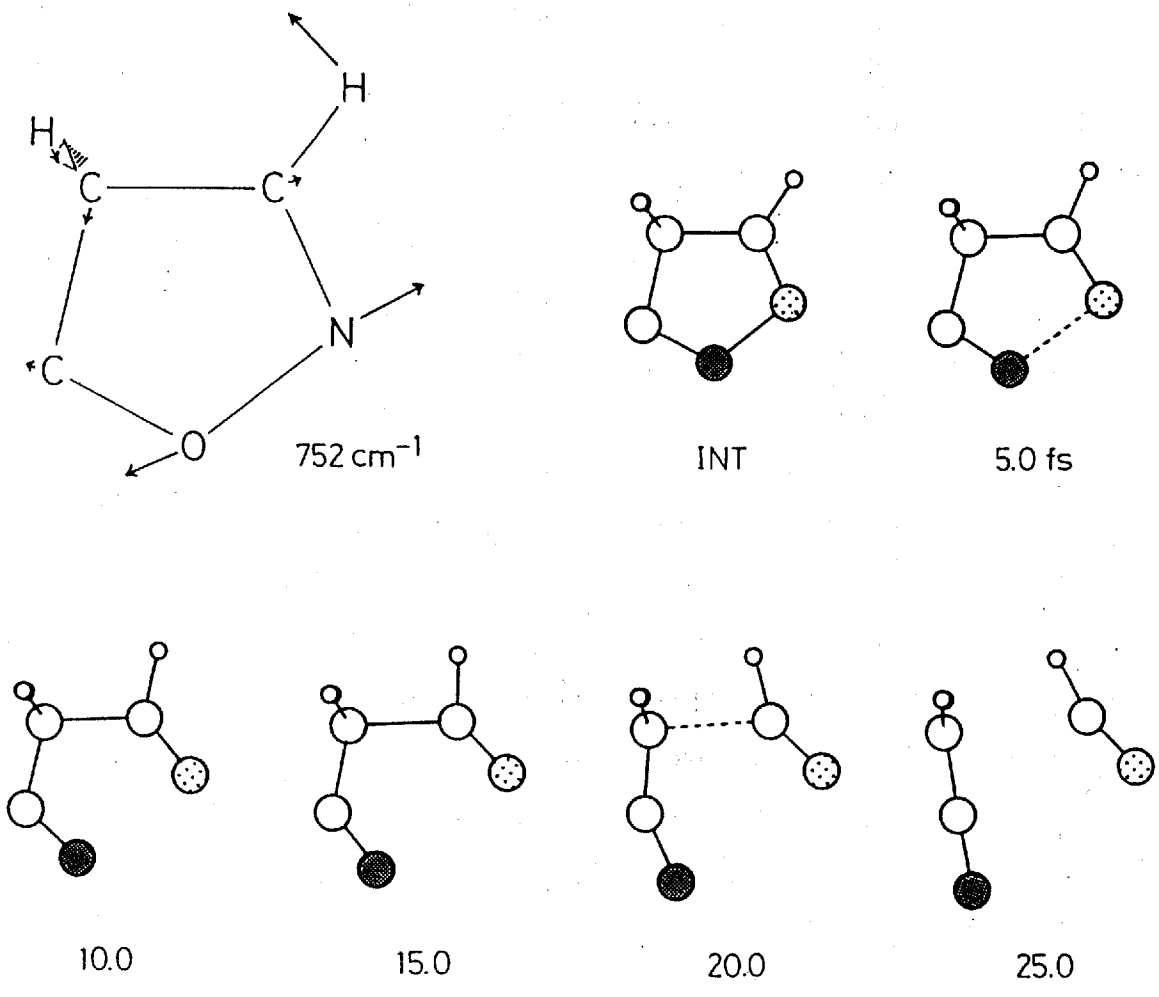

Figure 6.6: Same as Figure 6.5, except starting from the intermediate.

TABLE 6.1: Experimental and calculated structure parameters of isoxazole. Distances are in angstroms and angles in degrees.[a]

	expt.[b]	calcd.		
		3-21G	4-31G[c]	6-31G**
Distances				
O1–N2	1.398	1.441	1.418	1.360
N2–C3	1.314	1.292	1.290	1.281
C3–C4	1.427	1.436	1.431	1.428
C4–C5	1.358	1.338	1.339	1.340
O1–C5	1.346	1.360	1.350	1.321
C3–H	1.077	1.065	1.065	1.071
C4–H	1.076	1.062	1.063	1.068
C5–H	1.075	1.063	1.063	1.070
Angles				
O1–N2–C3	105.5	104.6	104.9	106.1
N2–C3–C4	112.0	112.9	112.4	111.7
C3–C4–C5	103.1	104.1	104.1	102.2
C4–C5–O1	110.5	110.4	109.8	110.6
C3–C4–H	128.5	127.3	127.4	128.9
C4–C3–H	128.8	127.5	128.1	128.8
C4–C5–H	133.4	132.9	133.4	133.0

[a] In labeling the constituent atoms, carbon adjacent to nitrogen is C3 and that adjacent to oxygen is C5.

[b] Microwave, Reference 68.

[c] Reference 69.

TABLE 6.2: Vibrational frequencies (cm^{-1}) of isoxazole.

symmetry species	mode	assignment	expt.[a]	calcd.		
				3-21G	4-31G[b]	6-31G**
A′	ν_1	CH str	3140	3502	3504	3466
	ν_2	CH str	3128	3474	3477	3442
	ν_3	CH str	3086	3452	3461	3421
	ν_4	ring str	1560	1732	1765	1802
	ν_5	ring str	1432	1563	1603	1637
	ν_6	ring str	1373	1501	1517	1543
	ν_7	CH i.p. bend	1330	1358	1377	1383
	ν_8	CH i.p. bend	1217	1252	1258	1278
	ν_9	ring breath	1128	1126	1151	1224
	ν_{10}	CH i.p. bend	1089	1099	1126	1117
	ν_{11}	ring str	1021	1030	1031	1044
	ν_{12}	ring i.p. deform	930	980	999	1010
	ν_{13}	ring i.p. deform	856	927	873	999
A″	ν_{14}	CH o.o.p. deform	1033	1116	1109	1047
	ν_{15}	CH o.o.p. deform	889	1066	1068	1030
	ν_{16}	CH o.o.p. deform	764	920	918	876
	ν_{17}	ring o.o.p. deform	632	698	702	703
	ν_{18}	ring o.o.p. deform	595	624	639	648

[a] Reference 70 .

[b] Reference 69.

TABLE 6.3: Total energies (hartrees), zero-point energies (kcal/mol), and relative energies (kcal/mol, +ZPE) relative to isoxazole.

species	HF/3-21G			HF/6-31G**		
	total energy	ZPE	ΔE	total energy	ZPE	ΔE
isoxazole	-243.210695	39.2	0	-244.594186	39.6	0
TS-1	-243.072288	34.8	82.5	-244.468762	35.9	75.0
INT	-243.133489	36.9	46.2	-244.515525	37.6	47.4
TS-2	-243.109883	35.2	59.3	-244.484945	35.2	64.2
TS-3	-243.074621	32.1	78.2	-244.460164	32.4	76.9
hydrogen cyanide	-92.35408[a]	11.5[a]	-18.3	-92.877138	11.2	-14.3
ketene	-150.87653[b]	21.8[b]		-151.728764	21.4	
acetonitrile	-131.191802	31.0	-51.6	-131.932496	30.5	-53.4
carbon monoxide	-112.09330[a]	3.3[a]		-112.737877	3.5	

[a] B. T. Luke et al., *J. Am. Chem. Soc.* **108**, 270 (1986).

[b] J. Andraos et al., *J. Mol. Struct.* **232**, 155 (1991).

Chapter 7

Concluding Remarks

7.1 General Conclusion

In the present thesis, we have investigated the origin of dynamical behaviors in the gas-phase unimolecular reactions, by considering a few reaction systems in which nitriles are thought to be produced by the thermal decompositions. Dynamical features such as selectivity in the reaction path are reasonably explained by the combined approach of the IRC and classical trajectory calculations.

Actually, in the trajectory calculations thermal vibrations of the molecule as well as the zero-point vibrations should be taken into account. Therefore, the way of giving the initial conditions in the present work may be rather oversimplified. (But, it is not until quite recently that some attempts have been made to incorporate zero-point vibrations into the trajectory calculation [73, 74].) Nevertheless, this treatment is believed to facilitate the understanding of the reaction dynamics, and to be a powerful strategy in the clarification of the dynamics of various reactions which show chemical activation.

But, before studying the dynamics of a reaction being concerned, it is essential to

determine the reaction channel(s). In Chapter 5, we have concluded both experimentally and theoretically that in the temperature range 1014–1300 K isomerization occurs for the thermal unimolecular reaction of pyruvonitrile, which was not reported in the past.

7.2 Thermal Decomposition of Ethyl Acetate

As stated in Chapter 2, the tendencies of the branching ratios for the consecutive reaction channels differ between the decomposition of ethyl formate and that of ethyl acetate. Saito et al.[22] explained that the result should come from the steric effect due to the presence of methyl group in the case of ethyl acetate. We agree this is a part of the reason, but there seems to exist the other factor as well. Ethyl acetate can take the form

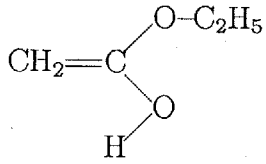

(7.1)

while ethyl formate cannot, and this form contributes to the preference of the dehydration channel. Moreover, the most recent theoretical studies [75, 76] indicate that the decomposition of acetic acid giving ketene and water involves a two-step process besides the direct dehydration, however the order of their importance is different. We think that additional experimental and theoretical studies would be worthwhile.

7.3 Other Reaction Systems

Lifshitz and co-workers [77, 78] also published the experimental studies on the reactions of methyl-substituted isoxazoles. In 5-methylisoxazole [77], the main reaction channel is similar to the one for the decomposition of isoxazole. On the contrary, isomerization has been reported to be the main thermal reaction of 3,5-dimethylisoxazole [78].

It is of interest to investigate the effect of the methyl group(s) on the reaction mechanism theoretically. This is a future task to be tackled.

References

(1) J. D. McDonald, *Ann. Rev. Phys. Chem.* **30**, 29 (1979).

(2) I. Oref and B. S. Rabinovitch, *Acc. Chem. Res.* **12**, 166 (1979).

(3) V. E. Bondybey, *Ann. Rev. Phys. Chem.* **35**, 591 (1984).

(4) P. J. Robinson and K. A. Holbrook, *Unimolecular Reactions* (Wiley-Interscience, New York, 1972), Chap. 8.

(5) W. Forst, *Theory of Unimolecular Reactions* (Academic Press, New York, 1973).

(6) D. C. Tardy and B. S. Rabinovitch, *Chem. Rev.* **77**, 369 (1977).

(7) J. W. Moore and R. G. Pearson, *Kinetics and Mechanism*, 3rd ed. (Wiley-Interscience, New York, 1981), p. 222.

(8) J. N. Butler and G. B. Kistiakowsky, *J. Am. Chem. Soc.* **82**, 759 (1960).

(9) R. E. Harrington, B. S. Rabinovitch, and H. M. Frey, *J. Chem. Phys.* **33**, 1271 (1960).

(10) B. E. Holmes and D. W. Setser, *J. Phys. Chem.* **82**, 2450, 2461 (1978).

(11) R. J. McCluskey and R. W. Carr, Jr., *J. Phys. Chem.* **82**, 2637 (1978).

(12) K. Eichler and H. Heydtmann, *Int. J. Chem. Kinet.* **13**, 1107 (1981).

(13) D. G. Boaglio, G. Arbilla, J. C. Ferrero, and E. H. Staricco, *Int. J. Chem. Kinet.* **21**, 1003 (1989).

(14) G. Arbilla, J. C. Ferrero, and E. H. Staricco, *Int. J. Chem. Kinet.* **24**, 619 (1992).

(15) (a) J. D. Rynbrandt and B. S. Rabinovitch, *J. Chem. Phys.* **54**, 2275 (1971).

(b) J. D. Rynbrandt and B. S. Rabinovitch, *J. Phys. Chem.* **75**, 2164 (1971).

(16) (a) B. S. Rabinovitch, J. F. Meagher, K.-J. Chao, and J. R. Barker, *J. Chem. Phys.* **60**, 2932 (1974).

(b) J. F. Meagher, K.-J. Chao, J. R. Barker, and B. S. Rabinovitch, *J. Phys. Chem.* **78**, 2535 (1974).

(17) F.-M. Wang and R. S. Rabinovitch, *Can. J. Chem.* **54**, 943 (1976).

(18) A. N. Ko, B. S. Rabinovitch, and K.-J. Chao, *J. Chem. Phys.* **66**, 1374 (1977).

(19) A. B. Trenwith and B. S. Rabinovitch, *J. Phys. Chem.* **86**, 3447 (1982).

(20) K. Saito, T. Kakumoto, H. Kuroda, S. Torii, and A. Imamura, *J. Chem. Phys.* **80**, 4989 (1984).

(21) K. Saito, K. Shimofuji, K. Adachi, M. Watanabe, and A. Imamura, *National Symposium on Shock Wave Phenomena*, 1989, ISAS, Sagamihara, Japan; p.65.

(22) K. Saito, T. Sasaki, I. Yoshinobu, and A. Imamura, *Chem. Phys. Lett.* **170**, 385 (1990).

(23) K. Okada, Graduation Thesis (in Japanese), Hiroshima University (1991).

(24) K. Saito, T. Kakumoto, and I. Murakami, *Chem. Phys. Lett.* **110**, 478 (1984).

(25) K. Fukui, *J. Phys. Chem.* **74**, 4161 (1970).

(26) (a) K. Fukui, *Acc. Chem. Res.* **14**, 363 (1981).

(b) K. Fukui, *Pure Appl. Chem.* **54**, 1825 (1982).

(27) (a) K. Fukui, S. Kato, and H. Fujimoto, *J. Am. Chem. Soc.* **97**, 1 (1975).

(b) S. Kato and K. Fukui, *J. Am. Chem. Soc.* **98**, 6395 (1976).

(c) S. Kato, H. Kato, and K. Fukui, *J. Am. Chem. Soc.* **99**, 684 (1977).

(28) (a) K. Fukui, A. Tachibana, and K. Yamashita, *Int. J. Quantum Chem., Quantum Chem. Symp.* **15**, 621 (1981).

(b) K. Fukui, *Int. J. Quantum Chem., Quantum Chem. Symp.* **15**, 633 (1981).

(29) K. Ishida, K. Morokuma, and A. Komornicki, *J. Chem. Phys.* **66**, 2153 (1977).

(30) H. B. Schlegel, *Adv. Chem. Phys.* **67**, 249 (1987).

(31) (a) B. C. Garrett, M. J. Redmon, R. Steckler, D. G. Truhlar, K. K. Baldridge, D. Bartol, M. W. Schmidt, and M. S. Gordon, *J. Phys. Chem.* **92**, 1476 (1988).

(b) K. K. Baldridge, M. S. Gordon, R. Steckler, and D. G. Truhlar, *J. Phys. Chem.* **93**, 5107 (1989).

(32) (a) M. Page and J. W. McIver, Jr., *J. Chem. Phys.* **88**, 922 (1988).

(b) M. Page, C. Doubleday, and J. W. McIver, Jr., *J. Chem. Phys.* **93**, 5634 (1990).

(33) (a) C. Gonzalez and H. B. Schlegel, *J. Chem. Phys.* **90**, 2154 (1989).

(b) C. Gonzalez and H. B. Schlegel, *J. Phys. Chem.* **94**, 5523 (1990).

(c) C. Gonzalez and H. B. Schlegel, *J. Chem. Phys.* **95**, 5853 (1991).

(34) (a) J.-Q. Sun and K. Ruedenberg, *J. Chem. Phys.* **99**, 5257 (1993).

(b) J.-Q. Sun and K. Ruedenberg, *J. Chem. Phys.* **99**, 5269 (1993).

(c) J.-Q. Sun, K. Ruedenberg, and G. J. Atchity, *J. Chem. Phys.* **99**, 5276 (1993).

(35) H. B. Schlegel, *J. Chem. Soc., Faraday Trans.* **90**, 1569 (1994).

(36) E. Kraka and T. H. Dunning, Jr., in *Advances in Molecular Electronic Structure Theory*, edited by T. H. Dunning, Jr. (JAI Press, Greenwich, 1990), Vol. 1, p. 129.

(37) G. L. Hofacker, *Z. Naturforsch.* **18a**, 607 (1963).

(38) (a) R. A. Marcus, *J. Chem. Phys.* **45**, 4500 (1966).

(b) R. A. Marcus, *J. Chem. Phys.* **49**, 2610, 2617 (1968).

(39) W. H. Miller, N. C. Handy, and J. E. Adams, *J. Chem. Phys.* **72**, 99 (1980).

(40) (a) W. H. Miller, in *Potential Energy Surfaces and Dynamics Calculations*, edited by D. G. Truhlar (Plenum Press, New York, 1981), p. 265.

(b) W. H. Miller, *J. Phys. Chem.* **87**, 3811 (1983).

(41) (a) S. K. Gray, W. H. Miller, Y. Yamaguchi, and H. F. Schaefer III, *J. Chem. Phys.* **73**, 2733 (1980).

(b) S. K. Gray, W. H. Miller, Y. Yamaguchi, and H. F. Schaefer III, *J. Am. Chem. Soc.* **103**, 1900 (1981).

(c) B. A. Waite, S. K. Gray, and W. H. Miller, *J. Chem. Phys.* **78**, 259 (1983).

(42) (a) S. M. Colwell, *Mol. Phys.* **51**, 1217 (1984).

(b) S. M. Colwell and N. C. Handy, *J. Chem. Phys.* **82**, 1281 (1985).

(43) K. Kamiya and K. Morokuma, *J. Chem. Phys.* **94**, 7287 (1991).

(44) W. H. Miller, in *The Theory of Chemical Reaction Dynamics*, edited by D. C. Clary (Reidel, Dordrecht, 1986), p. 27.

(45) D. G. Truhlar and B. C. Garrett, *Ann. Rev. Phys. Chem.* **35**, 159 (1986).

(46) D. G. Truhlar, R. Steckler, and M. S. Gordon, *Chem. Rev.* **87**, 217 (1987).

(47) D. G. Truhlar, F. B. Brown, R. Steckler, and A. D. Isaacson, in *The Theory of Chemical Reaction Dynamics*, edited by D. C. Clary (Reidel, Dordrecht, 1986), p. 285.

(48) M. J. Frisch, J. S. Binkley, H. B. Schlegel, K. Raghavachari, C. F. Melius, R. L. Martin, J. J. P. Stewart, F. W. Bobrowicz, C. M. Rohlfing, L. R. Kahn, D. J. Defrees, R. Seeger, R. A. Whiteside, D. J. Fox, E. M. Fluder, S. Topiol, and J. A. Pople, *GAUSSIAN 86*; Carnegie-Mellon University, Pittsburgh, 1986.

(49) M. J. Frisch, M. Head-Gordon, H. B. Schlegel, K. Raghavachari, J. S. Binkley, C. Gonzalez, D. J. Defrees, D. J. Fox, R. A. Whiteside, R. Seeger, C. F. Melius, J. Baker, R. L. Martin, L. R. Kahn, J. J. P. Stewart, E. M. Fluder, S. Topiol, and J. A. Pople, *GAUSSIAN 88*; Gaussian, Inc., Pittsburgh PA, 1988.

(50) M. J. Frisch, M. Head-Gordon, G. W. Trucks, J. B. Foresman, H. B. Schlegel, K. Raghavachari, M. Robb, J. S. Binkley, C. Gonzalez, D. J. Defrees, D. J. Fox, R. A. Whiteside, R. Seeger, C. F. Melius, J. Baker, R. L. Martin, L. R. Kahn, J. J. P.

Stewart, S. Topiol, and J. A. Pople, *GAUSSIAN 90*; Gaussian, Inc., Pittsburgh PA, 1990.

(51) M. J. Frisch, G. W. Trucks, M. Head-Gordon, P. M. W. Gill, M. W. Wong, J. B. Foresman, B. G. Johnson, H. B. Schlegel, M. A. Robb, E. S. Replogle, R. Gomperts, J. L. Andres, K. Raghavachari, J. S. Binkley, C. Gonzalez, R. L. Martin, D. J. Fox, D. J. Defrees, J. Baker, J. J. P. Stewart, and J. A. Pople, *Gaussian 92*; Gaussian, Inc., Pittsburgh PA, 1992.

(52) L. M. Raff and D. L. Thompson, in *Theory of Chemical Reaction Dynamics*, edited by M. Baer (CRC Press, Boca Raton, Florida, 1985), Vol. III, p. 1.

(53) J. J. P. Stewart, L. P. Davis, L. W. Burggraf, *J. Comput. Chem.* **8**, 1117 (1987).

(54) J. J. P. Stewart, MOPAC Ver.6, *QCPE Bull.* 9, 10 (1989); revised as Ver.6.01 by T. Hirano, University of Tokyo, for HITAC and UNIX machines, *JCPE Newsletter* 1, 10 (1989).

(55) (a) S. Kato and K. Morokuma, *J. Chem. Phys.* **73**, 3900 (1980).

(b) K. Morokuma and S. Kato, in *Potential Energy Surfaces and Dynamics Calculations*, edited by D. G. Truhlar (Plenum Press, New York, 1981), p. 243.

(c) S. Kato and K. Morokuma, *J. Chem. Phys.* **74**, 6285 (1981).

(56) (a) D. G. Truhlar and A. D. Isaacson, *J. Chem. Phys.* **77**, 3516 (1982).

(b) B. A. Waite, S. K. Gray, and W. H. Miller, *J. Chem. Phys.* **78**, 259 (1983).

(c) K. Yamashita and T. Yamabe, *Int. J. Quantum Chem., Quantum Chem. Symp.* 17, 177 (1983).

(57) K. Saito, K. Makishita, T. Kakumoto, T. Sasaki, and A. Imamura, *J. Phys. Chem.* **92**, 4371 (1988).

(58) R. N. Bennett, E. Jones, and P. D. Ritchie, *J. Chem. Soc.* **1956**, 2628.

(59) K. Saito, R. Ito, T. Kakumoto, and A. Imamura, *J. Phys. Chem.* 90, 1422 (1986).

(60) S. Glasstone, K. J. Laidler, and H. Eyring, *The Theory of Rate Processes* (McGraw-Hill, New York, 1941).

(61) J. I. Steinfeld, J. S. Francisco, and W. L. Hase, *Chemical Kinetics and Dynamics* (Prentice-Hall, Englewood Cliffs, 1989).

(62) S. Bell, G. A. Guirgis, J. Lin, and J. R. Durig, *J. Mol. Struct.* **238**, 183 (1990).

(63) B. T. Luke, J. A. Pople, M.-B. Krogh-Jespersen, Y. Apeloig, M. Karni, J. Chandrasekhar, and P. v. R. Schleyer, *J. Am. Chem. Soc.* **108**, 270 (1986).

(64) J. Andraos, A. J. Kresge, M. R. Peterson, and I. G. Csizmadia, *J. Mol. Struct.* **232**, 155 (1991).

(65) W. Fang, R. Liu, and X. You, *Chem. Phys. Lett.* **226**, 453 (1994).

(66) N-.y. Chang and C.-h. Yu, *Chem. Phys. Lett.* **242**, 232 (1995).

(67) A. Lifshitz and D. Wohlfeiler, *J. Phys. Chem.* 96, 4505 (1992).

(68) O. L. Stiefvater, P. Nösberger, and J. Sheridan, *Chem. Phys.* 9, 435 (1975).

(69) A. Komornicki, J. D. Goddard, and H. F. Schaefer III, *J. Am. Chem. Soc.* **102**, 1763 (1980).

(70) (a) S. Califano, F. Piacenti, and G. Speroni, *Spectrochim. Acta* **15**, 86 (1959).

(b) G. Adembri, G. Speroni, and S. Califano, *Spectrochim. Acta* **19**, 1145 (1963).

(71) W. J. Hehre, L. Radom, P. v. R. Schleyer, and J. A. Pople, *Ab Initio Molecular Orbital Theory* (Wiley-Interscience, New York, 1986).

(72) A. Doughty, G. B. Bacskay, and J. C. Mackie, *J. Phys. Chem.* **98**, 13546 (1994).

(73) T. D. Sewell, D. L. Thompson, J. D. Gezelter, and W. H. Miller, *Chem. Phys. Lett.* **193**, 512 (1992).

(74) K. F. Lim and D. A. McCormack, *J. Chem. Phys.* **102**, 1705 (1995).

(75) X. Duan and M. Page, *J. Am. Chem. Soc.* **117**, 5114 (1995).

(76) M. T. Nguyen, D. Sengupta, G. Raspoet, and L. G. Vanquickenborne, *J. Phys. Chem.* **99**, 11883 (1995).

(77) A. Lifshitz and D. Wohlfeiler, *J. Phys. Chem.* **96**, 7367 (1992).

(78) A. Lifshitz, D. Wohlfeiler, and C. Tamburu, *J. Phys. Chem.* **99**, 11436 (1995).

List of Publications

1. K. Saito, M. Watanabe, K. Adachi, M. Sugimoto, K. Okada, and G. Sasaki,
   "Vibrational states of carbon monoxide produced via successive unimolecular decomposition of relatively large molecules,"
   Proceedings of the 18th International Symposium on Shock Waves, Sendai (Jul., 1991), Springer-Verlag; pp. 747–752.

2. S. Okada, K. Yamasaki, H. Matsui, K. Saito, and K. Okada,
   "Studies on the reactions of CH(v=0 and 1) with NO and O_2,"
   Bull. Chem. Soc. Jpn. 66(4), 1004–1011(1993).

3. K. Saito, G. Sasaki, K. Okada, and S. Tanaka,
   "Unimolecular decomposition of pyruvic acid: An experimental and theoretical study,"
   J. Phys. Chem. **98**(14), 3756–3761(1994).

4. K. Okada, M. Sugimoto, and K. Saito,
   "A reaction-path dynamics approach to the thermal unimolecular decomposition of acetaldoxime,"
   Chem. Phys. **189**(3), 629–636(1994).*

5. K. Okada and K. Saito,
   "Thermal unimolecular reaction of pyruvonitrile: Experimental and computational study on the occurrence of isomerization,"
   J. Phys. Chem. 99(35), 13168–13172(1995).*

6. K. Okada and K. Saito,

"Reaction-path dynamics study of competing channels in the thermal unimolecular decomposition of isoxazole,"

J. Phys. Chem., submitted for publication.*

* The asterisk indicates the original paper of which contents are included in the thesis.